Solving hyperbolic conservation laws with active counteraction against numerical errors: Isothermal fixed-bed adsorption

Ju Weon Lee[1,*] and Andreas Seidel-Morgenstern[1,2]

[1] Max-Planck-Institute for Dynamics of Complex Technical Systems
Sandtorstr. 1, 39106 Magdeburg, 39106, Germany

[2] Institute of Process Engineering, Otto von Guericke University
Universitätsplatz 2, 39106 Magdeburg, Germany

*: Corresponding Author

Tel: +49 391 6110392

Fax: +49 391 6110521

Email: lee@mpi-magdeburg.mpg.de

Abstract

First-order partial differential equations are frequently applied for the simulation of adsorption and reaction processes. The numerous numerical methods available are typically applied without any further modifications despite of various well-known errors caused by, for example, numerical dissipation and crude approximations of certain phenomena. In this work, we analyzed a classical mixing cell model that is capable to simulate isothermal liquid chromatographic separation processes with incompressible mobile phases. This model corresponds to a 1D model of a chromatographic column discretized with a first-order finite volume method. It is our aim to counteract actively two errors, namely *numerical dispersion* (i.e. the second-order spatial derivative in truncation error) and *partition inconsistency* related to the nonlinear partition quantified by a competitive adsorption isotherm model. The new numerical method introduced in this article maintains characteristics of the first-order base scheme (non-oscillatory and conditionally stable) and offers enhanced accuracy (smaller numerical errors and improved description of shock waves). Furthermore, the method does not require solving the system of differential-algebraic equations that cause large matrix computations, but rather solves nonlinear equations ‘cell-by-cell’. The numerical routines can be easily parallelized to accelerate computation time with multi-core CPUs. To test the method developed, four-zone simulated moving bed adsorption as a challenging example was considered, which causes dynamically changing complex concentration profiles by periodic operation using several columns.

Keywords: Active Counteraction Scheme; Liquid Chromatography; Mixing Cell Model; Simulated Moving Bed; Generalized Langmuir Isotherms; Multi-Component Simulation

1. Introduction

The convection dominated component mass balances of columns packed with solid adsorbents is represented by the system of hyperbolic first-order partial differential equations. These equations provide very useful information to understand the complex retention behaviors of adsorbates and to design proper processes. Going beyond this basic model, chromatographic columns have been successfully modelled with various models of different complexities describing the most relevant thermodynamic and kinetic phenomena (Guiochon et al., 1994; Kim et al., 2017). In these models, the second-order spatial derivatives quantify unavoidable physical dispersion effects in the conservation laws. The partition equilibria between the two phases involved tend to be nonlinear and are coupled for higher concentrations. Therefore, there is no analytical solution available. Thus, proper numerical methods are required to solve this type of problems.

Often periodically operated multi-column configurations are applied to improve the efficiency of chromatographic separation processes with preparative purpose. To perform chromatographic separations with liquid mobile phases, one of the most promising continuous processes is the multi-column simulated moving bed (SMB) process. Since its introduction in the 1960s (Broughton et al., 1970), it is widely used in the petrochemical, fine chemical, sugar, and pharmaceutical industries. The conventional SMB process was developed for the separation of binary or pseudo-binary mixtures using four distinct zones that are divided by two inlets and two outlets, so that it consists at least four columns (at least one column per zone). Because of its structural and operational complexities, mechanistic approaches are commonly applied to the process design, and process simulation is unavoidable (Wu et al., 1998; Migliorini et al., 1999; Lee et al., 2014). The control of the SMB process for dynamic optimization has been recently studied to resolve model-system mismatch problems (Klatt et al., 2002; Andrade Neto et al., 2016; Lee et al., 2018).

To solve the mass balance equations of chromatographic single or multi-column processes, many methods have been addressed for the discretization of the conservation laws. Various simulation tools were developed. Leão and Rodrigues (2004) compared four different PDE solver packages for the simulation of the true moving bed system. One of the simplest method is the finite difference

method (FDM) exploiting a first-order upwind discretization scheme (UDS). Higher order schemes were introduced to reduce numerical errors, such as the Lax-Wendroff scheme and the biased upwind discretization schemes (Courant et al., 1952; Lax & Wendroff, 1960; Loureiro & Rodrigues, 1991). Other approaches are the finite volume method (FVM) with flux limiters based on total variation diminishing (TVD) to avoid the spurious oscillations (LeVeque, 2002) and the finite element method (FEM) with moving nodes to reduce computational load (Coimbra et al., 2000). Since oscillatory errors cause critical problems in the simulation of physical systems, weighted essentially non-oscillatory (WENO) schemes were introduced (Liu et al., 1994). However, rigorous mass balance models discretized with the above-mentioned high-order and high-resolution schemes have two significant limitations;

- As the column model becomes more rigorous and complex, the number of parameters to be measured or estimated increases, e.g. parameters for mass transfer model.
- High-order and high-resolution numerical schemes can provide accurate solutions only if complex numerical routines and larger computation resources are invested.

Due to these restrictions, a rather simple 1D process model discretized with the FDM exploiting the first-order UDS is widely used to simulate the chromatographic processes. This approach can be applied matching the spatial node numbers to the experimentally determined numbers of theoretical plates (NTP) of the column in order to passively introduce the second-order numerical error matching the corresponding physical dispersion effect (Rouchon et al., 1987; Czok & Guiochon, 1990a; Czok & Guiochon, 1990b; Heuer et al., 1995). This method requires only relatively short computation times, and is rather accurate, when all components have identical or similar dispersion coefficients (or NTPs) and the migration velocities of the solutes do not change dynamically with concentrations.

In this work, the first-order UDS, which is non-oscillatory and conditionally stable if it satisfies the Courant–Friedrichs–Lewy (CFL) condition (Courant et al., 1928), was considered to quantify the corresponding numerical errors using Taylor series expansions. The error of second-order spatial derivatives were actively modulated to compensate the physical dispersion effect. An additional model-scheme mismatch error, designated in this article as *partition inconsistency* error caused by

non-linear competitive adsorption isotherms, was quantitatively evaluated. A numerically efficient method was developed and demonstrated based on counteracting both errors simultaneously.

2. Numerical Scheme

For isothermal liquid chromatographic processes with an incompressible mobile phase (the mobile phase flow-rate is constant), one of the simplest mass balance models is the following one-dimensional hyperbolic system of first-order partial differential equations,

$$\frac{\partial c_i}{\partial t} + F\frac{\partial q_i}{\partial t} + u_L\frac{\partial c_i}{\partial z} = 0 \;\; with \;\; F = \frac{(1-\varepsilon)}{\varepsilon}, \;\; i \in \mathbf{N}_S \tag{1}$$

where c_i and q_i are respectively the concentration of solute i in the mobile and stationary phases, F is the phase ratio, ε is the void fraction of the chromatographic column, u_L is the interstitial velocity of the mobile phase, and $\mathbf{N}_S$ is the set of solutes. Assuming that two phases are thermodynamically equilibrium (typically quantified using adsorption isotherm models), the stationary phase concentrations are functions of the mobile phase concentrations, $q_i = f(c_i | i \in \mathbf{N}_S)$. By substituting q by c, the mass balance equation, Eq. (1) can be rewritten as a canonical first-order wave equation (or a convection equation),

$$\frac{\partial \kappa_i c_i}{\partial t} + u_L\frac{\partial c_i}{\partial z} = 0 \tag{2-1}$$

and the partition parameter, κ_i is a function of $\mathcal{D}q_i/\mathcal{D}c_i$, which is the total derivative of q_i with respect to c_i,

$$\kappa_i = \left(1 + F\frac{\mathcal{D}q_i}{\mathcal{D}c_i}\right) \;\; with \;\; \frac{\mathcal{D}q_i}{\mathcal{D}c_i} = \sum_{j\in\mathbf{N}_S}\left(\frac{dc_j}{dc_i}\frac{\partial q_i}{\partial c_j}\right) \tag{2-2}$$

Assuming that the partition parameters, κ_i are constant, Eq. (2-1) can be rewritten as,

$$\frac{\partial c_i}{\partial t} + u_{S,i}\frac{\partial c_i}{\partial z} = 0 \;\; with \;\; u_{S,i} = \frac{u_L}{\kappa_i} \tag{2-3}$$

This equation describes waves travelling with the constant migration velocity, $u_{S,i}$. However, the partition parameters imply the thermodynamic equilibria as shown in Eq. (2-2). Thus, the migration

velocity may vary while the solutes travel through the column. However, in convection-dominant systems, $u_{S,i}$ can never be faster than u_L. This means that the partition parameters are physically meaningful only if they are equal or greater than 1. Eq. (2-1) is the well-known fundamental equilibrium model of chromatography and capable to simulate essential features of liquid chromatographic separation processes (DeVault, 1943; Guiochon et al., 1994).

While the equilibrium model (also known as the ideal model), Eq. (1) describes dominant mass transfer by convection and retention by adsorption in the chromatographic column, band-broadening effects, which are mainly caused by diffusion/dispersion and limited mass transfer between two phases, is still missing. In order to achieve higher accuracy, it is a simple and efficient way to introduce a second-order longitudinal dispersion term that captures unavoidable band broadening effects through diffusive-transport phenomena taking place inside of packed columns into Eq. (2-1). Thus, it is called the equilibrium-dispersive model and can be rewritten as,

$$\frac{\partial \kappa_i c_i}{\partial t} + u_L \frac{\partial c_i}{\partial z} = D_{L,i} \frac{\partial^2 c_i}{\partial z^2} \tag{3-1}$$

where $D_{L,i}$ is the apparent longitudinal dispersion coefficient of solute i, which implies above mentioned band-broadening effects. It is the goal of this work to provide an efficient numerical solution for this type of 1D column mass balance equations, which form the core of reliable single and multi-column models. For this, we will exploit below the well-known analogy between Eq. (3-1) and a corresponding model considering the column as a series of a finite number of sequentially connected mixing cells (MC) (Martin & Synge, 1941; Craig, 1944; Kramers & Alberda, 1953). Using Laplace transforms, the MC scheme was extended to solve the dynamic models that includes various mass transfers between two phases in linear chromatography (Villermaux, 1987). Assuming established equilibria, the discretized mass balance equations of a specific cell *n* in such a cascade are:

$$\frac{\kappa_i(n,t+\Delta t)\bar{c}_i(n,t+\Delta t) - \kappa_i(n,t)\bar{c}_i(n,t)}{\Delta t} + u_L \frac{\bar{c}_i(n,t) - \bar{c}_i(n-1,t)}{\Delta z_n} = 0, \quad n \in \mathbf{N}_C = \{1, \dots, N_C\} \tag{3-2}$$

The introduced average mobile phase concentrations, $\bar{c}_i$ are

$$\bar{c}_i(n,t) = \frac{1}{\Delta z_n} \int_{(n-1)\Delta z_n}^{n\Delta z_n} c_i(z,t)dz, \quad \sum_{n \in \mathbf{N}_C} \Delta z_n = L_C$$

Δt and Δz_n are respectively the discretized time step and the length of cell n, L_C is the column length, N_C denotes the last cell in the column, and $\mathbf{N}_C$ is the set of discretized cells in the column.

The second-order derivative terms, which describe the physical dispersion effect, are omitted in computation in the MC scheme. However, the numerical errors are quantified and manipulated to compensate the missing physical dispersion terms. Therefore, solving Eq. (3-1) with the MC scheme is equivalent to solving hyperbolic conservation laws, Eq. (1). In the next section, we will analyze Eq. (3-2) in more detail and exploiting connections to Eq. (3-1).

2.1.Mixing cell model with first-order upwind scheme

Assuming that the cell lengths, Δz_n are all identical and $\kappa_i(n,t)$ is locally constant to $\bar{\kappa}_i(n,t)$ in t to $t + \Delta t$, Eq. (3-2) can be rewritten as a convection equation with constant parameters,

$$\bar{\kappa}_i(n,t)\frac{\bar{c}_i(n,t+\Delta t)-\bar{c}_i(n,t)}{\Delta t} + u_L\frac{\bar{c}_i(n,t)-\bar{c}_i(n-1,t)}{\Delta z} = 0 \quad (4\text{-}1)$$

Assuming that the migration velocities of solutes are locally constant between the cells n and $n-1$, this equation is equivalent to,

$$\frac{\bar{c}_i(n,t+\Delta t)-\bar{c}_i(n,t)}{\Delta t} + \bar{u}_{S,i}(n,t)\frac{\bar{c}_i(n,t)-\bar{c}_i(n-1,t)}{\Delta z} = 0 \quad (4\text{-}2)$$

where $\bar{u}_{S,i}(n,t)$ is the locally constant migration velocity of the solute i. The necessary condition to make Eqs. (4-1) and (4-2) identical is,

$$\bar{\kappa}_i(n,t)\bar{u}_{S,i}(n,t) = u_L \quad (4\text{-}3)$$

Note that $\bar{\kappa}_i$ is constant for a certain cell in the time interval Δt, i.e. the representative value of $\kappa_i(n,t)$ and $\kappa_i(n,t+\Delta t)$. Furthermore, $\bar{u}_{S,i}$ is constant for neighbored cells at a certain time, i.e. the representative value of $u_{S,i}(n-1,t)$ and $u_{S,i}(n,t)$.

In FVMs with flux limiters (LeVeque, 2002), two constant migration velocities at the inlet and outlet of the cell were used, so that this method provides second-order accuracy when the solution is smooth (e.g. in case of rarefaction waves) or the first-order accuracy when the solution is steep or

discontinued (e.g. in case of shock waves). However, FVMs do not guarantee that Eqs. (4-1) and (4-2) are identical. Let us call this type of numerical error an *inconsistency* error, which we will further discuss later.

Using Taylor series expansions of the time and spatial derivatives for the mean fluid phase concentrations,

$$\bar{c}_i(n,t+\Delta t) = \bar{c}_i(n,t) + \Delta t \frac{\partial \bar{c}_i(n,t)}{\partial t} + \frac{(\Delta t)^2}{2}\frac{\partial^2 \bar{c}_i(n,t)}{\partial t^2} + \frac{(\Delta t)^3}{6}\frac{\partial^3 \bar{c}_i(n,t)}{\partial t^3} + \cdots \quad (5\text{-}1)$$

and

$$\bar{c}_i(n,t) = \bar{c}_i(n-1,t) - \Delta z \frac{\partial \bar{c}_i(n,t)}{\partial z} + \frac{(\Delta z)^2}{2}\frac{\partial^2 \bar{c}_i(n,t)}{\partial z^2} - \frac{(\Delta z)^3}{6}\frac{\partial^3 \bar{c}_i(n,t)}{\partial z^3} + \cdots \quad (5\text{-}2)$$

The error of second-order derivatives can be quantified. The right hand sides of the following equations allows quantifying numerical errors of the MC scheme with the locally constant partition parameter,

$$\bar{\kappa}_i \frac{\partial \bar{c}_i}{\partial t} + u_L \frac{\partial \bar{c}_i}{\partial z} = \frac{u_L \Delta z}{2}(1-\mathcal{C}_i)\frac{\partial^2 \bar{c}_i}{\partial z^2} + \frac{u_L (\Delta z)^2}{6}\left(3\mathcal{C}_i - 2\mathcal{C}_i{}^2 - 1\right)\frac{\partial^3 \bar{c}_i}{\partial z^3} + \cdots, \quad \mathcal{C}_i = \frac{u_L \Delta t}{\bar{\kappa}_i \Delta z} \quad (6\text{-}1)$$

and with the locally constant migration velocity,

$$\frac{\partial \bar{c}_i}{\partial t} + \bar{u}_{S,i}\frac{\partial \bar{c}_i}{\partial z} = \frac{\bar{u}_{S,i}\Delta z}{2}(1-\mathcal{C}_i)\frac{\partial^2 \bar{c}_i}{\partial z^2} + \frac{\bar{u}_{S,i}(\Delta z)^2}{6}\left(3\mathcal{C}_i - 2\mathcal{C}_i{}^2 - 1\right)\frac{\partial^3 \bar{c}_i}{\partial z^3} + \cdots, \quad \mathcal{C}_i = \frac{\bar{u}_{S,i}\Delta t}{\Delta z} \quad (6\text{-}2)$$

where $\mathcal{C}_i$ is the Courant number of solute i. Note that the Courant numbers are a function of the locally constant partition parameter, $\bar{\kappa}_i$, or the locally constant migration velocity, $\bar{u}_{S,i}$, respectively. The Courant number may violate the CFL condition if $\bar{\kappa}_i$ or $\bar{u}_{S,i}$ values are physically inconsistent. The even-order derivative terms on the right hand side cause smearing errors and the odd-order derivative terms cause wiggle errors (LeVeque, 2007). Later we will consider again the second-order physical dispersion term, see Eq. (3). The parameter of the second-order derivative in the truncation error of Eq. (6-2) contains the locally constant migration velocity, the representative migration velocity of the neighbored cells n and $n-1$ at time t. This means that the truncation errors of the neighbored cell mass balances are coupled, i.e. it is complicated to quantify the numerical errors cell-by-cell. Because

of this reason, let us consider Eq. (6-1) for further development of numerical approach and introduce here the second-order numerical error as,

$$\mathcal{O}_{D,i} = D_{N,i}\frac{\partial^2 \bar{c}_i}{\partial z^2} \;\; with \;\; D_{N,i} = \frac{u_L \Delta z}{2}(1 - \mathcal{C}_i) \tag{7}$$

where, $\mathcal{O}_{D,i}$ and $D_{N,i}$ are the *numerical dispersion* error and the *numerical dispersion* coefficient (analog to the physical dispersion) of solute i, respectively.

To retrieve the original convection equation, Eq. (3), the accumulation term should satisfy the following condition,

$$\frac{\partial \kappa_i \bar{c}_i}{\partial t} = \bar{\kappa}_i \frac{\partial \bar{c}_i}{\partial t} + \mathcal{O}_{P,i} \tag{8-1}$$

and the locally constant partition parameter can be approximated as,

$$\bar{\kappa}_i = 1 + F\frac{\partial_t \bar{q}_i}{\partial_t \bar{c}_i}, \;\; \frac{\partial_t \bar{q}_i}{\partial_t \bar{c}_i} = \lim_{\Delta t \to 0} \frac{\Delta_t \bar{q}_i}{\Delta_t \bar{c}_i} = \lim_{\Delta t \to 0} \frac{\bar{q}_i(n,t+\Delta t) - \bar{q}_i(n,t)}{\bar{c}_i(n,t+\Delta t) - \bar{c}_i(n,t)} \tag{8-2}$$

where $\bar{q}_i$ is the average concentration of solute i in the stationary phase of cell n and $\mathcal{O}_{P,i}$ is the *partition inconsistency* error. Note that the condition same as Eq. (8-1) can be considered for the convection term of compressible and/or variable density mobile phase conditions, $\frac{\partial u_L \bar{c}_i}{\partial z}$, even though it is not considered in this article. In general, the *partition inconsistency* error is zero if a physically meaningful partition coefficient ($\bar{\kappa}_i \geq 1$) exists. However, $\bar{\kappa}_i$ represents lumped partition information during Δt and may be inconsistent in case of competitive adsorption. If the partition parameter is smaller than 1 ($\mathcal{C}_i > 1$), it violates the CFL condition and the solution is unstable. In this case, smaller time steps should be applied to obtain physically meaningful partition parameters as described in Appendix A. To avoid this complex and time consuming computation, let us consider a *partition inconsistency* error if the partition parameter, $\bar{\kappa}_i$ violates the following physically meaningful bounds,

$$1 \leq \lfloor \bar{\kappa}_i \rfloor \leq \bar{\kappa}_i \leq \lceil \bar{\kappa}_i \rceil \tag{9-1}$$

where the special brackets $\lfloor x \rfloor$ and $\lceil x \rceil$ denote the physically possible minimum and maximum values of x, respectively. From these criteria, the mentioned *partition inconsistency* error can be quantified as,

$$\mathcal{O}_{P,i} = \begin{cases} \frac{\partial \kappa_i \bar{c}_i}{\partial t} - \lfloor \bar{\kappa}_i \rfloor \frac{\partial \bar{c}_i}{\partial t}, & \bar{\kappa}_i < \lfloor \bar{\kappa}_i \rfloor \\ 0, & \lfloor \bar{\kappa}_i \rfloor \leq \bar{\kappa}_i \leq \lceil \bar{\kappa}_i \rceil \\ \frac{\partial \kappa_i \bar{c}_i}{\partial t} - \lceil \bar{\kappa}_i \rceil \frac{\partial \bar{c}_i}{\partial t}, & \bar{\kappa}_i > \lceil \bar{\kappa}_i \rceil \end{cases} \tag{9-2}$$

or

$$\mathcal{O}_{P,i} = \begin{cases} F \frac{\Delta \bar{q}_i}{\Delta t} - F \left\lfloor \frac{\Delta_t \bar{q}_i}{\Delta_t \bar{c}_i} \right\rfloor \frac{\Delta \bar{c}_i}{\Delta t}, & \bar{\kappa}_i < \lfloor \bar{\kappa}_i \rfloor \\ 0, & \lfloor \bar{\kappa}_i \rfloor \leq \bar{\kappa}_i \leq \lceil \bar{\kappa}_i \rceil \\ F \frac{\Delta \bar{q}_i}{\Delta t} - F \left\lceil \frac{\Delta_t \bar{q}_i}{\Delta_t \bar{c}_i} \right\rceil \frac{\Delta \bar{c}_i}{\Delta t}, & \bar{\kappa}_i > \lceil \bar{\kappa}_i \rceil \end{cases} \tag{9-3}$$

Now, the quantified *partition inconsistency* error can be expressed as a function of the concentrations in the stationary phase.

The discretized convection equation differs from the original convection equation, Eq. (2-1) due to two introduced distinct numerical errors, $\mathcal{O}_{D,i}$ and $\mathcal{O}_{P,i}$.

$$\frac{\partial \kappa_i \bar{c}_i}{\partial t} + u_L \frac{\partial \bar{c}_i}{\partial z} = \mathcal{O}_{D,i} + \mathcal{O}_{P,i} \tag{10-1}$$

The left hand side is the original convection equation that should be zero, and the right hand side captures the numerical errors caused by the MC scheme. Note that the numerical errors (the right hand side) arise only if the original convection equation (the left hand side) is numerically solved with the MC scheme. This means that the concentration variables inside of the numerical error formulae, $\mathcal{O}_{D,i}$ and $\mathcal{O}_{P,i}$ should be quantified and subtracted from the numerical solution of the left hand side. Thus, the numerical routines for solving Eq. (10-1) should be divided into two sequential steps; at first, the left hand side is numerically solved with the MC scheme, and then the numerical errors are quantified by solving the right hand side in order to allow error modulation. For linear isotherms (constant partition and non-competitive, i.e. $\mathcal{O}_{P,i} = 0$), this equation can be rewritten as,

$$\kappa_i \frac{\partial \bar{c}_i}{\partial t} + u_L \frac{\partial \bar{c}_i}{\partial z} = D_e \frac{\partial^2 \bar{c}_i}{\partial z^2}, \quad D_e = \frac{u_L H}{2} = \lim_{\mathcal{C} \to 0} D_{N,i} = \frac{u_L \Delta z}{2} \tag{10-2}$$

where D_e is the apparent dispersion coefficient (note that it is assumed that all solutes have the same dispersion coefficient) and H is the height of equivalent theoretical plate. If the Courant number is small enough, the apparent dispersion coefficient can be replaced to the *numerical dispersion*

coefficient, i.e. the *numerical dispersion* can compensate physical dispersion effect. This is one special case of the passive counteraction schemes applied, e.g. by (Czok & Guiochon, 1990a; Czok & Guiochon, 1990b). The general discretized convection equation, Eq. (10-1) provides a useful formula for treating incompressible chromatographic separation problems that may include mass transfer resistance and even reactions occurring in the mobile and stationary phases inside of a mixing cell.

2.2.Modified dispersion applying a fictitious dispersion coefficient

Let us handle now the physical dispersion term only as a certain portion of *numerical dispersion* error that should not eliminated from the solution. Let us subtract the numerical errors identified above from the physical dispersion term in Eq. (3-1);

$$\frac{\partial \kappa_i \bar{c}_i}{\partial t} + u_L \frac{\partial \bar{c}_i}{\partial z} = D_{L,i} \frac{\partial^2 \bar{c}_i}{\partial z^2} - \mathcal{O}_{D,i} - \mathcal{O}_{P,i} \qquad (11\text{-}1)$$

or

$$\frac{\partial \kappa_i \bar{c}_i}{\partial t} + u_L \frac{\partial \bar{c}_i}{\partial z} = D_{F,i} \frac{\partial^2 \bar{c}_i}{\partial z^2} - \mathcal{O}_{P,i} \qquad (11\text{-}2)$$

where $D_{F,i}$ is the newly introduced fictitious dispersion coefficient ($D_{F,i} = D_{L,i} - D_{N,i}$). Then the right hand side of Eq. (11) indicates the numerical error compensation (including physical dispersion) caused in the convection equation. The sign of the fictitious dispersion coefficient indicates which dispersion effect is dominant. If the physical dispersion coefficient is smaller than the *numerical dispersion* coefficient ($D_{F,i} < 0$), the numerical solution of the convection equation is too dispersed. In this case, the numerical solution of the convection equation should be further compressed (or dispersed if $D_{F,i} > 0$) exploiting the fictitious dispersion coefficient (Figure 1).

To quantify the mass transferred in accordance with the fictitious dispersion between two neighbored cells, let us consider an isolated two-cell system. The transferred mass by fictitious dispersion between the cells n and $(n + 1)$ is proportional to the concentration gradient. Assuming that the concentration gradient and the fictitious dispersion coefficient are locally constant in the time interval, Δt, the masses transferred by fictitious dispersion between two neighbored cells, $M_{D,i}$ is,

$$M_{D,i}(n,t) = -\varepsilon A_C \overline{D}_{F,i}(n,t)\left\{\frac{\bar{c}_i(n+1,t)-\bar{c}_i(n,t)}{\Delta z}\right\}\Delta t \quad (12\text{-}1)$$

The average fictitious dispersion coefficient obtained from the average Courant number is,

$$\overline{D}_{F,i}(n,t) = D_{L,i}(u_L) - \frac{u_L \Delta z}{2}\left\{1 - \frac{\mathcal{C}_i(n+1,t)+\mathcal{C}_i(n,t)}{2}\right\} \quad (12\text{-}2)$$

where A_C is the cross-sectional area of the column, and $\overline{D}_{F,i}$ is the average fictitious dispersion coefficient of solute i. The physical dispersion coefficient is a function of the mobile phase flow-rate (however, it was assumed that the physical dispersion coefficient is constant in this work) and the *numerical dispersion* coefficient is a function of the Courant number. In the mixing cell model, $\Delta t \leq \Delta z/u_L$ and $\lfloor D_F \rfloor = -\lfloor D_N \rfloor = -u_L \Delta z/2$. Therefore, $2\overline{D}_{F,i}\Delta t/(\Delta z)^2 \geq -1$. Analogue to that the CFL condition for the second-order derivative term should hold, $\left|2\overline{D}_{F,i}\Delta t/(\Delta z)^2\right| \leq 1$. Under compression conditions ($\overline{D}_{F,i} < 0$), the same discretized time step can be used. However, the discretized time may be further divided to several smaller time step in dispersion condition ($\overline{D}_{F,i} > 0$) to satisfy the CFL condition, $\left|M_{D,i}\right| \leq |\bar{c}_i(n+1,t) - \bar{c}_i(n,t)|$.

2.3.Active counteraction against both identified numerical errors

The considered numerical errors discussed above, namely the *numerical dispersion and partition inconsistency* errors, can be quantitatively subtracted from the numerical solution of the MC formulation of the convection equation. For this, the numerical computation method needs to be divided in two steps. The first step is solving the convection equation with the MC scheme, and the second step is applying the active counteraction (AC) against the numerical errors.

Step 1: MC Scheme

Appling uniformly the same Δz and $\Delta t = \Delta z/u_L$ to Eq. (3-2), the discretized convection equation of cell n at time t becomes,

$$\left\{\bar{c}_i^{\#}(n,t) + F\bar{q}_i^{\#}(n,t)\right\}\Delta z = \{\bar{c}_i(n,t) + F\bar{q}_i(n,t)\}\Delta z + \{\bar{c}_i(n-1,t) - \bar{c}_i(n,t)\}\frac{\Delta z}{\varepsilon} \quad (13\text{-}1)$$

where $\bar{c}_i^{\#}$ and $\bar{q}_i^{\#}$ are respectively the equilibrium cell concentrations of solute i in the mobile and stationary phases after Δt exclusively due to convection. The boundary conditions, the inlet and outlet concentrations are given as,

$$\begin{cases}\bar{c}_i(1,t) = \bar{c}_{Inlet,i} \\ \bar{c}_{Outlet,i} = \bar{c}_i(N_C,t)\end{cases} \quad (13\text{-}2)$$

where the subscripts, $Inlet$ and $Outlet$ denote the column inlet and outlet, respectively. Depending on the isotherm model, $\bar{c}_i^{\#}$ and $\bar{q}_i^{\#}$ can be analytically (in case of linear isotherm models) or numerically (in case of non-linear isotherm models) solved cell-by-cell. The results of solving the pure convection equations, $\bar{c}_i^{\#}$ and $\bar{q}_i^{\#}$, provide the initial concentrations for the AC scheme applied in the second step.

Step 2: AC Scheme

In this step, the numerical errors caused in the above MC scheme are quantified and effectively eliminated from the solution of MC scheme. To incorporate the *partition inconsistency* error, the maximum and minimum bounds of $\bar{\kappa}_i$ and the corresponding error $\mathcal{O}_{P,i}$ should be obtained from the thermodynamic properties of the considered physical system. For example, we consider below a quite flexible and widely applicable generalized competitive Langmuir isotherm (Mazzotti, 2006) as,

$$\bar{q}_i = \frac{a_i\bar{c}_i}{1+\sum_{j\in\mathbf{N}_S} p_j b_j \bar{c}_j}, \quad p_j = \begin{cases}1, & Langmuirian \\ -1, & Anti-Langmuirian\end{cases} \quad (14\text{-}1)$$

The necessary condition for positive quantities of adsorbed solutes is,

$$1 + \sum_{j\in\mathbf{N}_S} p_j b_j \bar{c}_j > 0 \quad (14\text{-}2)$$

where a_i and b_i are the Langmuir isotherm parameters of solute i and p_j is the assignment constant of solute j. If any of p_j is –1, this isotherm model is only valid in the concentration range where the

denominator is greater than zero. Since the type of adsorption isotherm behavior varies with p_j, it is not easy to identify the maximum bound of $\Delta_t \bar{q}_i / \Delta_t \bar{c}_i$ if any of the p_j is –1.

$$if\ \forall p_j = 1,\ \ \lfloor \bar{\kappa}_i \rfloor = 1 \leq \bar{\kappa}_i \leq 1 + Fa_i = \lceil \bar{\kappa}_i \rceil \tag{15-1}$$

or

$$if\ \exists p_j = -1,\ \ \lfloor \bar{\kappa}_i \rfloor = 1 \leq \bar{\kappa}_i \tag{15-2}$$

As shown in Eq. (9-3), the modulation of *partition inconsistency* error can be applied only to the stationary phase concentration while the modulation of *numerical dispersion* error is applied to the mobile phase concentration. Because of infinite upper bounds for anti-Langmuirian isotherms, only the lower bounds were considered, cf. Eq. (15-2).

$$if\ \bar{\kappa}_i < 1,\ \ \begin{cases} \bar{\kappa}_i = 1 \\ \Delta \bar{q}_i^{\#}(n,t) = \bar{q}_i^{\#}(n,t) - \bar{q}_i(n,t) \end{cases} \tag{16}$$

where $\Delta \bar{q}_i^{\#}$ is the stationary phase concentration form of the *partition inconsistency* error ($= \frac{\Delta t}{F} \mathcal{O}_{P,i}$). Note that a physically feasible $\bar{\kappa}_i$ value exist in general ($\Delta \bar{q}_i^{\#}(n,t) = 0$). Thus, the *numerical dispersion* coefficient, $D_{N,i}$ can be quantified. On the other hand, $\bar{\kappa}_i$ is enforced to be 1 and all numerical error can be compensated by the *partition inconsistency* error ($D_{N,i} = 0$). Note that the locally constant partition parameter is related to the locally constant migration velocity due to the necessary condition, Eq. (4-3). If the *partition inconsistency* error arises, the mass in the stationary phase should be manipulated to satisfy $\bar{\kappa}_i = 1$. This means that the mass in the stationary phase that occur partition inconsistency, $\Delta \bar{q}_i^{\#}$ should be eliminated from the cell. To keep the total mass balance, we handled the quantified *partition inconsistency* error as a fictitious dispersion in the stationary phase to spread out the neighbored cells. The corresponding fictitious stationary phase fluxes between the cells n and $n+1$, $\delta_{\bar{q},i}(n,t)$ are,

$$\delta_{\bar{q},i}(n,t) = \frac{\Delta u_{S,i}(n,n+1,t) \Delta \bar{q}_i^{\#}(n+1,t)}{\Delta u_{S,i}(n,n+1,t) + \Delta u_{S,i}(n+1,n+1,t)} - \frac{\Delta u_{S,i}(n,n,t) \Delta \bar{q}_i^{\#}(n,t)}{\Delta u_{S,i}(n,n,t) + \Delta u_{S,i}(n,n-1,t)},\ \ n \in \mathbf{N}_C - \{N_C\} \tag{17-1}$$

and the fictitious stationary phase fluxes at both ends of the column are assumed to be zero,

$$\delta_{\bar{q},i}(0,t) = \delta_{\bar{q},i}(N_C,t) = 0 \quad (17\text{-}2)$$

Thus, the difference of the migration velocities between cells n and m is,

$$\Delta u_{S,i}(n,m,t) = \left|u_{S,i}(n,t) - \bar{u}_{S,i}(m,t)\right| \quad (17\text{-}3)$$

Using the modified dispersion model with the fictitious dispersion coefficient, the fictitious mobile phase flux between the cells n and $n+1$, $\delta_{\bar{c},i}(n,t)$ is,

$$\delta_{\bar{c},i}(n,t) = \frac{M_{D_i}(n,t)}{\varepsilon A_C \Delta z} = -\left(\frac{\Delta t}{(\Delta z)^2}\overline{D}_{F,i}\right)\Delta\bar{c}_i^{\#}(n,t), \quad n \in \mathbf{N}_C - \{N_C\} \quad (18\text{-}1)$$

and the fictitious mobile phase fluxes at both ends of the column are assumed to be zero,

$$\delta_{\bar{c},i}(0,t) = \delta_{\bar{c},i}(N_C,t) = 0 \quad (18\text{-}2)$$

With the fictitious concentration fluxes in the mobile and stationary phases, the pure convection solution using MC scheme (Step 1) can be updated to,

$$\bar{c}_i^{\#}(n,t+\Delta t) = \bar{c}_i^{\#}(n,t) + \delta_{\bar{c},i}(n-1,t) - \delta_{\bar{c},i}(n,t) \quad (19\text{-}1)$$

$$\bar{q}_i^{\#}(n,t+\Delta t) = \bar{q}_i^{\#}(n,t) + \delta_{\bar{q},i}(n-1,t) - \delta_{\bar{q},i}(n,t) \quad (19\text{-}2)$$

The updated concentrations, $\bar{c}_i^{\#}(n,t+\Delta t)$ and $\bar{q}_i^{\#}(n,t+\Delta t)$ may violate physical boundaries (causing negative concentrations and/or over compressed concentrations by unexpected profile compression). To avoid these violations, the following mass flux limiters can be applied.

$$\left\lfloor \bar{c}_i^{\#}(n,t+\Delta t)\right\rfloor \le \bar{c}_i^{\#}(n,t+\Delta t) \le \left\lceil \bar{c}_i^{\#}(n,t+\Delta t)\right\rceil \quad (20\text{-}1)$$

and

$$0 \le \bar{q}_i^{\#}(n,t+\Delta t) \quad (20\text{-}2)$$

To obtain the solute migration velocities, one should consider the total derivative of the isotherms with respect to the mobile phase concentrations as shown in Eq. (2-2**)**. However, since there is no concentration gradient in the mixing cell, let us assume that the solute migration velocities in each cell can be obtained from the partial derivatives as,

$$\hat{u}_{S,i}(n,t) = \frac{u_L}{1+F\frac{\partial \bar{q}_i(n,t)}{\partial \bar{c}_i(n,t)}} \tag{21-1}$$

where $\hat{u}_{S,i}(n,t)$ is the migration velocity of solute i in cell n at time t. The position of discretized concentration profiles in the cell n after Δt can be obtained as shown in **Figure 2**. Therefore, possible upper and lower bounds of $\bar{c}_i^{\#}(n, t + \Delta t)$ are obtained as,

$$\left\lceil \bar{c}_i^{\#}(n, t + \Delta t) \right\rceil = \max \left(\begin{array}{l} \frac{\hat{u}_{S,i}\left(n-\frac{1}{2},t\right)\bar{c}_i(n-1,t)+0.25\{\hat{u}_{S,i}\left(n-\frac{1}{2},t\right)-\hat{u}_{S,i}(n-1,t)\}\{\bar{c}_i(n,t)-\bar{c}_i(n-1,t)\}}{\hat{u}_{S,i}\left(n-\frac{1}{2},t\right)} \\ \frac{\{u_L-\hat{u}_{S,i}\left(n-\frac{1}{2},t\right)\}\bar{c}_i(n,t)+0.25\{\hat{u}_{S,i}(n,t)-\hat{u}_{S,i}\left(n-\frac{1}{2},t\right)\}\{\bar{c}_i(n-1,t)-\bar{c}_i(n,t)\}}{u_L-\hat{u}_{S,i}\left(n-\frac{1}{2},t\right)} \end{array} \right) \tag{21-2}$$

and

$$\left\lfloor \bar{c}_i^{\#}(n, t + \Delta t) \right\rfloor = \min \left(\begin{array}{l} \frac{\hat{u}_{S,i}\left(n-\frac{1}{2},t\right)\bar{c}_i(n-1,t)+0.25\{\hat{u}_{S,i}\left(n-\frac{1}{2},t\right)-\hat{u}_{S,i}(n-1,t)\}\{\bar{c}_i(n,t)-\bar{c}_i(n-1,t)\}}{\hat{u}_{S,i}\left(n-\frac{1}{2},t\right)} \\ \frac{\{u_L-\hat{u}_{S,i}\left(n-\frac{1}{2},t\right)\}\bar{c}_i(n,t)+0.25\{\hat{u}_{S,i}(n,t)-\hat{u}_{S,i}\left(n-\frac{1}{2},t\right)\}\{\bar{c}_i(n-1,t)-\bar{c}_i(n,t)\}}{u_L-\hat{u}_{S,i}\left(n-\frac{1}{2},t\right)} \end{array} \right) \tag{21-3}$$

where $\hat{u}_{S,i}\left(n-\frac{1}{2},t\right)$ is the average migration velocity of solute i in the cells $n-1$ and n (= $\left\{\hat{u}_{S,i}(n,t)-\hat{u}_{S,i}(n-1,t)\right\}/2$). In case of rarefaction waves, a stepwise profile is broadened, but a stepwise profile is overlapped under shock wave conditions. Therefore, $\delta_{\bar{c},i}$ for compression ($\overline{D}_{F,i} < 0$) is allowed to have bigger value (shock wave condition, but restricted to smaller value in rarefaction wave condition). The mass flux caused by profile dispersion is not limited (the dimensionless fictitious dispersion coefficient can be smaller than –1, and the size of mass flux can greater than the mass difference in the mobile phase of neighbored cells, Figure 1). Therefore, the maximum time step for the profile dispersion was set to $(\Delta z)^2/\left(4D_{F,i}\right)$ (equivalent to 0.5 of the dimensionless dispersion coefficient in Figure 1). After refining the calculations using the numerical errors, newly assigned concentrations of the mobile and stationary phases are not thermodynamically equilibrium. Therefore, finally the following equations have to be solved cell-by-cell.

$$\bar{c}_i(n, t + \Delta t) + F\bar{q}_i(n, t + \Delta t) = \bar{c}_i^{\#}(n, t + \Delta t) + F\bar{q}_i^{\#}(n, t + \Delta t) \tag{22}$$

In summary, the described two-step MC-AC scheme quantifies two numerical errors of the explicit MC scheme, and actively modulate these errors to compensate the physical dispersion effect.

Therefore, good accuracy may be achievable compared to the MC scheme. In the MC scheme, the masses accumulated in the cells can be explicitly assigned cell-by-cell, and in the AC scheme, the quantified numerical errors can be explicitly modulated cell-by-cell. Newton-Raphson method (Burden et al., 1993) was used for two steps of nonlinear adsorption equilibria, Eqs. (13-1) and (22). Nonlinear solvers are iterative and require $(\#\mathbf{N}_S)$ by $(\#\mathbf{N}_S)$ matrix inversion. This means that the nonlinear solver is the most time-consuming numerical routine, but can be executed cell-by-cell. Therefore, the computation time of MC-AC scheme is twice as the computation time of MC scheme. However, the approach suggested does not require any higher order scheme to improve the solution accuracy. It is easy to be implemented for parallel computation.

2.4.Case study: Four-zone simulated moving bed chromatography

To test the proposed MC-AC scheme instead of a single-column batch process, we chose a challenging periodically operated multi-column continuous process. In multi-column continuous process, the concentration profiles are built up by superposing newly fed profiles on the existing profiles. Therefore, superposed complex wave patterns can be developed.

One of the most powerful liquid chromatographic separation process is four-zone SMB that is applicable for the continuous separation of binary and pseudo-binary mixtures. Figure 3 illustrates the periodic operation of four-zone closed-loop SMB. Each zone is divided by four external stream ports, *Feed*, *Desorbent*, *Extract*, and *Raffinate*. The ports are periodically switched to the next position toward the same direction of the mobile phase flow, so that the stationary phase flow is simulated to the opposite direction of the mobile phase flow. With this simulated counter-current flow of the mobile and stationary phases, the feed mixture is continuously separated into two outlets, *Extract* and *Raffinate*. In the *Extract*, the more-retained solute is collected, whereas the less-retained solute is collected in the *Raffinate*. Because of continuous feeding of mixture, newly fed mixture profiles are superposed on the early fed mixture profiles, and the internal concentration profiles are finally built up to cyclic steady-state (CSS) profiles. The four-zone SMB process has five operating conditions, four

mobile phase flow-rates in the zones and one port switching interval. The periodically changing boundary conditions of the zones are,

$$c_{Z1,Inlet,i} = \frac{Q_{Z4}c_{Z4,Outlet,i}+(Q_{Z1}-Q_{Z4})c_{Dsrb,i}}{Q_{Z1}} = \frac{Q_{Z4}c_{Z4,Outlet,i}}{Q_{Z1}} \quad (23\text{-}1)$$

$$c_{Z2,Inlet,i} = c_{Z1,Outlet,i} \quad (23\text{-}2)$$

$$c_{Z3,Inlet,i} = \frac{Q_{Z2}c_{Z2,Outlet,i}+(Q_{Z3}-Q_{Z2})c_{Feed,i}}{Q_{Z3}} \quad (23\text{-}3)$$

$$c_{Z4,Inlet,i} = c_{Z3,Outlet,i} \quad (23\text{-}4)$$

where the subscripts, $Feed$ and $Dsrb$ denote the *Feed* and *Desorbent* ports, the subscripts, $Z1$ to $Z4$ denote the zones 1 to 4, and Q is the volumetric flow-rate. A solute-free solvent was used at the Desorbent port, i.e. $\bar{c}_{Dsrb,i} = 0$.

In this work, the main goal is not finding conditions to separate the feed mixture, but to test the proposed numerical scheme. Therefore, several sets of operating conditions were arbitrary chosen. Hereby it was intended to generate internal concentration profiles that have sharp and superposed shocks. Four connected columns (one column per zone) were used. The dimension of the columns considered was 2.5 cm × 10 cm (I.D. × Length). The total void fraction, ε was = 0.69 (the phase ratio, F = 0.45). To visualize the internal concentration profiles of the chosen SMB system, the normalized axial distance, z/L_C, from the desorbent port toward the liquid phase flow direction was set as an x-axis. Thus, the concentration profiles, $\bar{c}_i(z/L_C)$ over the zone 1 (0 to 1 of z/L_C) through the zone 4 (3 to 4 of z/L_C) can be generated. To obtain the profiles at CSS, the process simulation was done up to 20th port switching interval.

From these profiles, a hodograph analysis can be applied. As described in Section 2.3, the MC-AC scheme requires the second equilibrium computations, Eq. (22) to modulate numerical errors quantified with the simple approximation to avoid complex computation (Appendix A). This means that the characteristics of the first-order PDEs, Eq. (A-3) may be violated if the second step AC scheme modulate the numerical errors improperly. To evaluate the numerical solution of MC-AC

scheme, the hodograph analysis was carried out for binary mixture systems (two-dimensional plane), which can be analytically solved.

For the convection equations of binary system (the more-retained solute, A; the less-retained solute, B), the characteristic directions on the hodograph, $\zeta_{\pm}$ can be analytically obtained from the following equations in Riemann problem (Rhee et al., 1989),

$$\zeta_{\pm}(c_A, c_B) = \frac{dc_B}{dc_A} = \frac{1}{2}\left(\frac{\partial q_A}{\partial c_B}\right)^{-1}\left\{\left(\frac{\partial q_B}{\partial c_B} - \frac{\partial q_A}{\partial c_A}\right) \pm \sqrt{\left(\frac{\partial q_B}{\partial c_B} - \frac{\partial q_A}{\partial c_A}\right)^2 + 4\frac{\partial q_A}{\partial c_B}\frac{\partial q_B}{\partial c_A}}\right\} \quad (24)$$

The points on the hodograph plane, (c_A, c_B) has two characteristic directions. For the generalized Langmuir isotherms, the sign of direction varies in terms of the assignment parameters, p_i. For example, in Langmuirian isotherms case ($\partial q_A/\partial c_B < 0$ and $\partial q_B/\partial c_A < 0$), the characteristic directions; ζ_- is positive and ζ_+ is negative. However, the signs are opposite ($\zeta_- > 0$ and $\zeta_+ < 0$) in anti-Langmuirian case ($\partial q_A/\partial c_B > 0$ and $\partial q_B/\partial c_A > 0$).

Based on the equivalent true moving bed analysis (Storti et al., 1993), the hodograph lines around the ports follow the characteristic directions of the corresponding port concentrations if the inlet and outlet concentrations of the port are the same. For well-posed CSS profiles, i.e. the concentrations at the *Desorbent* port are zero, the hodograph lines can be obtained from the following equations and two axes ($c_A = 0$ and $c_B = 0$) assuming that $c_{Z2,Outlet,i} = c_{Z3,Inlet,i}$,

$$c_B - c_{Z3,Inlet,B} = \zeta_{\pm}\left(c_{Z3,Inlet,A}, c_{Z3,Inlet,B}\right)\left(c_A - c_{Z3,Inlet,A}\right) \quad (25)$$

where $c_{Z3,Inlet,A}$ and $c_{Z3,Inlet,B}$ represent the concentrations at the *Feed* port. This hodograph analysis can assess if a numerical method provides thermodynamically consistent solutions.

2.5.Implementation of computation routines

To implement the proposed numerical method, all computation routines were coded with C++ language and compiled with Microsoft Visual C++® compiler (Ver. 19, included in Microsoft Visual Studio® 2015 Express Edition). To solve the nonlinear equation system, the Newton-Raphson method

was used. For parallel mixing cell computation (Figure 4), Microsoft Parallel Pattern Library® (PPL) was used. All computation time was measured in CPU time, and the Amdahl's law (Amdahl, 1967) was used to measure the efficiency of parallelized computation.

$$S(N_{CU}) = \frac{N_{CU}}{N_{CU}-(N_{CU}-1)r_{Parallel}} \tag{26}$$

where, S is the speedup ratio compared to the speed of single computation unit, N_{CU} is the number of computation unit involved, $r_{Parallel}$ is the ratio of parallelized computation.

To compare the numerical method proposed in this work to other numerical methods, a commercial simulator, Aspen Chromatography® (Ver. 8.8, AspenTech Inc. USA) was used for applying the first-order upwind scheme (UDS), fourth-order biased upwind scheme (BUDS), and the finite volume method with OSPRE flux limiter (OSPRE). The commercial simulator solves the differential-algebraic system of equations (DAEs) with an ODE solver. In this work, fourth-order adaptive Runge-Kutta method was chosen to solve ODEs (Appendix B). Since it is not easy to compare the computation times obtained from disparate computation routines, the relative computation times of the MC-AC and OSPRE schemes to the first-order upwind scheme with 50 cells (nodes) per column were compared. Since there is no available analytical solution for non-linear isotherms system, reference solutions obtained by the MC scheme with $\#\mathbf{N}_C$ = 10000 cells per column were used to calculate L^1 and L^∞ errors as,

$$L^1 = \frac{\sum_{i\in\mathbf{N}_S, n\in\mathbf{N}_C}\left(\frac{\left|\bar{c}_{Cal,i}(n)-\bar{c}_{Ref,i}(n)\right|}{c_{Feed,i}}\right)}{(\#\mathbf{N}_S)(\#\mathbf{N}_C)} \tag{27-1}$$

$$L^\infty = \max_{i\in\mathbf{N}_S, n\in\mathbf{N}_C}\left(\frac{\left|\bar{c}_{Cal,i}(n)-\bar{c}_{Ref,i}(n)\right|}{c_{Feed,i}}\right) \tag{27-2}$$

where the subscripts, Cal and Ref denote the calculated numerical solution and the corresponding reference solution, respectively.

3. Results and Discussion

As mentioned above, the internal profiles of SMB process are built up inside of the columns from cycle to cycle until a cyclic steady-state (CSS) is reached. If the operating conditions are well

chosen to avoid any recycling of solutes through the *Desorbent* port, the internal concentration profiles are located around the *Feed* port, and various shapes of shock and rarefaction wave combinations can be developed. To evaluate the accuracy and efficiency of the proposed MC-AC scheme, two different operating conditions were analyzed assuming typical parameters of the generalized Langmuir isotherms, Eq. (14-1) as shown in Table 1. To generate reasonable retention of solutes, the Henry's constant of the most-retained solute, a_A was set to 4.0 and the b_i parameters were set to have the same maximum adsorption capacity, i.e. $a_i/b_i = a_j/b_j$. Then the adsorption isotherm equations are thermodynamically consistent. The feed concentrations and the isotherm parameters, $c_{Feed,i}$ and b_i were arbitrarily chosen to describe significant nonlinear behaviors, which form dispersed rarefaction and sharp shock waves. In most of SMB processes, the mobile phase condition is isocratic (constant and identical solvent compositions in the feed and desorbent streams), so that the isotherm model considered in this work does not contain any parameter for adsorbable solvent. However, the numerical method introduced in this article may be also applicable to the solvent-gradient SMB process (Abel et al., 2002, 2004) with appropriate isotherm models for gradient elution.

The port switching interval, t_S was fixed to 4 min. Thus, the operating conditions could be specified by fixing four internal zone flow-rates, Q_{Z1} to Q_{Z4}. In Langmuirian isotherms, the front end of elution band forms shock. Therefore, the shapes of shock fronts can be changed by the flow-rates of the zones 3 and 4. In the SMB-Condition 1, the flow-rates of the zones 3 and 4 were chosen to form the superposed multiple shocks in the zone 3 (2 to 3 of z/L_C). On the other hand, the steep-and-narrow shocks were formed in the zone 4 (3 to 4 of z/L_C) in the SMB-Condition 2 (cf. Figure 5). These two conditions were used to evaluate the MC-AC scheme in the following Sections 3.1 to 3.5.

3.1.Mixing cell scheme (MC scheme)

At first, the solutions of MC scheme were compared in various numbers of cells. Since the second-order numerical error term is the most dominant in truncation error, the right hand side of Eq. (6), so that the numerical solutions are more dispersed when smaller number of cells was used in the

MC scheme. Figure 5 illustrates the computed internal concentration profiles at the end of 20th port switching interval by the MC scheme with various numbers of cells for the Conditions 1 and 2 (Table 1). The *Desorbent* and *Feed* ports are located at 0 and 2 of z/L_C.

For Condition 1 (Figure 5a), the more-retained solute profile was not reached to *Raffinate* port and the ports were switched to the next positions, so that the multiple superposed shocks were formed in the zone 3 (between *Feed* and *Raffinate* ports, 2 to 3 of z/L_C). The concentrations at the outlet of the zone 2 were different from the feed concentrations ($c_{Z2,Outlet,A} < c_{Feed,A}$ and $c_{Z2,Outlet,B} > c_{Feed,B}$), so that small humps were observed (the point A in Figure 5a).

For Condition 2 (Figure 5b), the front shocks of both solutes pass through the zone 3, and the steep-and-narrow shock wave profiles were formed in the zone 4 (between *Raffinate* and *Desorbent* ports, 3 to 4 of z/L_C). In CSS, the zone 3 is completely saturated with the feed concentrations, and the adsorption and desorption profiles are formed in the zones 4 and 2, respectively. Therefore, this condition is a typical Riemann problem.

As the number of cells increases, the numerical errors, which occur the numerical dispersion effects, were reduced in the MC scheme. This means that the numerical solution becomes closer to the exact solution of the equilibrium model. Therefore, we computed the internal concentration profiles of Conditions 1 and 2 using the MC scheme with $\#\mathbf{N}_C$ = 10000, and used them as the reference solutions of the equilibrium model. All simulations were performed up to 20 port switching intervals, which were sufficient to reach the CSS, to obtain the solution in CSS.

3.2.Mixing cell with active counteraction scheme (MC-AC scheme)

To reduce the numerical errors, the suggested AC scheme was applied. Figure 6 shows how the MC-AC scheme compresses the internal concentration profiles for the cases of 20 and 200 cells. Since the size of cell, Δz in Eq. (4), represents the resolution of numerical solutions, the solution with 20 cells provides slightly dispersed profiles. If any *numerical dispersion* takes place, the solutions should have broadened elution bands like Figure 5. However, the elution bands in Figure 6 was

broadened as much as the cell size, Δz increased, i.e. the resolution of numerical solution decreased, and only 200 cells were large enough to obtain the same accuracy as the reference solutions.

The MC-AC scheme requires one more step of cell equilibration, Eq. (22) for the numerical error treatment. This means that the characteristics of the first-order PDEs, Eq. (25) may be broken if the numerical errors are not correctly modulated. The profiles of the reference and MC-AC solutions were compared on the hodograph plane as shown in Figure 7 (cf. Figure B-2 in Appendix B). The hodograph lines obtained from Eq. (25) represent the exact solution ($\#\mathbf{N}_C = \infty$).

In Condition 2, a typical Riemann problem, the characteristic lines at the feed concentrations were perfectly matched with the hodograph lines of the reference solution (Lines BC and CD in Figures 7b and 7d). The point C indicates the feed port concentrations, which are the same as the feed concentrations in Condition 2.

In Condition 1, a small curvature (the point E in Figures 7a and 7c) was observed on the line BC of the reference solution because of asymptotic CSS characteristics (Zhong et al., 1996). Since the zone 2outlet and the zone 3 inlet concentrations were not the same at the end of port switching interval, small humps (indicated at the point A in Figure 5a) were located in the zone 2 and transferred in the rarefaction waves during next port switching intervals. However, it was difficult to identify in the solutions of the MC-AC scheme because of insufficient resolutions (barely seen in Figure 7c).

In both tested conditions, the hodograph lines of 20 cells were deviated from the reference lines because of poor resolution (Figures 7a and 7b). However, the hodograph lines of $\#\mathbf{N}_C$ = 200 cells perfectly matched to the reference lines (Figures 7c and 7d). This means that the second computation step for the AC scheme does not violate the characteristics of the governing PDEs.

Due to the additional second step for the AC scheme, the computation time of the MC-AC scheme was almost doubled (Figure 8a) compared to the MC scheme. This additional second step for the AC scheme must be performed after the MC scheme, so that the extra computation time for the AC scheme was not shortened in parallel computation. However, the MC-AC scheme can be easily

implemented for the parallel computation. Even though the parallel computation routines were not fully optimized, 78% of computation routines were parallelized (Figure 8b).

All computations were done in a desktop PC with Intel i7® CPU. This CPU supports the simultaneous multi-threading (SMT) technology (HyperThreading®). This means that up to two computation units (threads) can be assigned to the same CPU core to improve efficiency of CPU usage. Since all parallelized computation routine uses the same part of CPU core (arithmetic-logical and floating-point units), and a certain overhead is required for scheduling the parallelized computation units, the computation speed of SMT was even slower than the speed of the single threading.

3.3.Comparing the MC-AC scheme with other schemes

As shown above, the MC-AC scheme can improve the accuracy of the MC scheme by efficient modulation of the numerical errors. However, many commercial process simulation tools are already available exploiting high-order and high-resolution schemes. To compare the developed scheme with well-established schemes, three different numerical schemes were considered, namely the first-order UDS, the fourth-order BUDS, and the FVM with the OSPRE flux limiter. The recently developed high-order WENO schemes were not considered in this work because they have many variations and are still under development (Jiang & Shu, 1996; von Lieres & Andersson, 2010). These schemes use high-order (usually the fifth-order or higher) scheme with weighted sub-stencils, so that they provide highly accurate and non-oscillatory solutions with heavy load of computation and proper weight factors of sub-stencils (Alhumaizi, 2004; Črnjaric-Žić et al., 2004; John & Novo, 2012).

The three above-mentioned schemes were compared with the MC-AC scheme with the same number of cells. For the commercial simulator, the same number of spatial nodes was set. Figure 9 compared four tested numerical schemes in Condition 1, respectively. As expected, the UDS scheme provides significantly dispersed solution, and the BUDS scheme provides spurious oscillations around steep shock waves. The FVM with OSPRE flux limiter (the second-order scheme) provides relatively good numerical solution and it is comparable to the MC-AC scheme. The discretization methods use

the Taylor's series expansion to approximate the time and spatial derivatives in the PDEs, so that their solution implies the numerical dissipation errors that need to be eliminated by proper high-order schemes or alternative flux limiters based on TVD. This means that it is difficult to avoid smearing or spurious oscillation errors if the number of nodes or cells are not big enough.

In Figures. 10c and 10d, the OSPRE scheme generates significantly dispersed profiles when only 20 spatial nodes were used. However, the MC-AC scheme actively subtract the quantified numerical errors during each cell computation, so that the numerical solutions obtained from 20 cells have much less smearing errors without spurious oscillation. As mentioned in Section 2.1, the FVMs with flux limiters take the average fluxes that may cause an inconsistency error, so that the positions of shock waves are shifted as the number of spatial nodes decreased. However, the AC scheme quantifies *partition inconsistency* errors to eliminate them from the solution and to obtain the physically feasible Courant number for the profile compression or dispersion. Therefore, the positions of shock waves are the same even though the number of cells is very small (Figures 10a and 10b).

Figure 11 shows the L^1 and L^∞ errors of the MC-AC and OSPRE schemes for Conditions 1 and 2. The OSPRE scheme has the second-order accuracy. However, this accuracy decreases near the shock wave to obtain non-oscillatory solution. Because of this accuracy switching by the flux limiter (the second-order accuracy is switched to the first-order accuracy around sharp shock, so that the errors near shock waves are more significant than other errors as shown in Figure 9c), the slopes of the L^1 error for the OSPRE scheme are close to 1. The MC-AC scheme also has the first-order accuracy because of the base MC scheme. Therefore, the slopes of the L^1 error for the MC-AC scheme are also close to 1, but errors at the same $\#\mathbf{N}_C$ were much smaller than the OSPRE scheme. In the reference solution, the solution has stepwise shock waves, so that the L^∞ error was not significantly improved (improved L^∞ accuracy cannot be achieved if the same or better resolution is not used compared to the reference solution). Moreover, the OSPRE scheme finds wrong shock wave position because of the *partition inconsistency* error.

To compare the computation speeds of the coded routines and the commercial simulator, the relative speed of the MC-AC scheme to the speed of the MC scheme with 50 cells,

{Speed of MC − AC Scheme}/{Speed of MC Scheme with 50 cells}, and the relative speed of the OSPRE scheme to the speed of the UDS scheme with 50 spatial nodes, {Speed of OSPRE Scheme}/{Speed of UDS Scheme with 50 nodes}, were compared. Figure 12 shows the comparisons of the MC-AC and OSPRE scheme performances. Since the flux limiter (not only the OSPRE scheme) limits the solution gradient when the solution is close to shock, the performance gap between the MC-AC and OSPRE schemes in Condition 1 (superposed multi-step shock wave condition) was greater than Condition 2. All four performance lines have the similar slopes (0.52 ~ 0.63) in Conditions 1 and 2, so that the MC-AC scheme is approximately 10 times faster or approximately 1/5 smaller L^1 error level than the OSPRE scheme at the same L^1 error level or at the same computation speed, respectively.

The MC-AC scheme cannot overcome the convergency characteristics of the base MC scheme, i.e. the first-order accuracy. However, it can significantly remove the two numerical errors that are quantified by the AC scheme, and accelerates computation with small number of cells to provide relatively good solution.

3.4.Potential of reducing the cell numbers with MC-AC scheme

In Sections 3.1 to 3.3, we considered only the first-order PDEs solution, i.e. Eq. (3-1) without physical dispersion, $D_{L,i}$ = 0. However, in preparative and production scale process, the convection is not strongly dominant. This means that the elution bandwidth is significantly broadened by physical dispersion, and the precise prediction of broadened bandwidth is important to design or control chromatographic separation process. Therefore, it is desirable that the numerical solutions obtained from different number of cells or spatial nodes should provide the same degree of dispersion. This means that the numerical errors caused in different number of cells or spatial nodes should be the same.

As tested in Section 3.3, only the MC-AC scheme provides accurate elution bandwidths, so that Figure 13 compared the dispersed numerical solutions obtained by the MC-AC scheme with various number of cells. Two physical dispersion coefficients considered, 0.1 cm^2/min and 1.0

cm^2/min were arbitrary chosen because those are typical lower and upper bounds of apparent dispersion coefficients in preparative chromatography. Because of poor resolution caused by large volume of cell, only the numerical solutions with 10 cells provide more dispersed concentration profiles around the steep shock wave (Figures 13a and 13b). This means that the *numerical dispersion* errors are effectively modulated to compensate the physical dispersion effect. Consequently, the model parameters estimated with different number of cells can be identical or very close for the same physical system. Therefore, the parameters estimated with this scheme are more reliable than the ones from other numerical methods that essentially contains specific numerical errors.

In Table 2, the contributions of numerical computation routines of the MC-AC scheme were compared in terms of the number of routine calls and the average iteration number of the nonlinear solver. In the MC-AC scheme, there are two serial computation routines, the convection routine in the MC scheme ($N_{\Delta t}$ is the number of MC routine calls) and the numerical error modulation routine in the AC scheme ($R_{\Delta t}$ is the number ratio of AC routine calls to $N_{\Delta t}$). Since the discretized time step for convection was decided by the length of the cell ($\Delta t = \Delta z/u_L$), $N_{\Delta t}$ values were all the same for different $D_{L,i}$ cases. However, the discretized time step for the numerical error modulation routine is related to the CFL condition for the second-order dispersion term as described in Section 2.2 so that the time step smaller than the convection routine may be applied if $D_{L,i}$ too large compared to the time step (Note $\Delta t = \Delta z/u_L$) . Under well determined N_C conditions ($R_{\Delta t}$ < 5.0), the computation speeds of different $D_{L,i}$ cases were close each other. In $R_{\Delta t}$ > 1.0 conditions, the discretized time step is divided into several sub-steps to satisfy $2\overline{D}_{F,i}\Delta t/(\Delta z)^2 \leq 0.5$ and additional serialized computation steps are required for the profile dispersion in the AC scheme. However, dispersed profiles decreases steep jump of concentrations, so that the nonlinear solver can find the solution in less iterations and compensate extra computation time. If $\#\mathbf{N}_C$ is too small ($R_{\Delta t}$ > 5.0), the reduced computation time of the nonlinear solver cannot compensate increased computation time for profile dispersion (the nonlinear solver requires at least ~5 average iterations in these cases), and the computation speed decreases.

Consequently, the ratio quantity, $R_{\Delta t}$ value can be used to determine a proper number of cells. If , $R_{\Delta t} = 1$, the fictitious dispersion coefficient is negative, and the profiles are compressed by the AC scheme. This means that the number of cells is smaller than the conventional MC scheme with the passive counteraction scheme, and the error of numerical solution is only proportional to the resolution (the size of cells). The computation speed is not significantly slowed down in $R_{\Delta t} \leq 5.0$. Therefore, one can decide the right number of cells (the size of cells) corresponding to the desired accuracy (resolution) up to $R_{\Delta t} = 5.0$.

3.5.Simulation of diverse dispersion system with MC-AC scheme

In the cases studied above, both solutes have the same physical dispersion coefficients, and it is possible to solve the PDEs using the passive counteraction, that is the same as the MC scheme with designated cell size. However, it is not possible to acquire suitable numerical solution if the solutes have quite diverse physical dispersion coefficients as described in Figure 14. We tested two different dispersed systems for the Conditions 1 and 2. In Figures 14a and 14c, the less-retained solute has quite large physical dispersion coefficient, $D_{L,B}$ = 1.0, and the more-retained solute has no dispersion. The opposite cases were shown in Figures 14a and 14c. This dispersion difference can be realized by the selective mass transfer rates between two phases. It can be a critical factor for separations if convection is not strongly dominant to the migration velocity (Guiochon et al., 1994). To assess the front and rear ends of the elution bands, the numerical solutions of the diverse physical dispersion systems obtained using the MC-AC scheme with 50 cells were compared with the reference solutions (solution for non-dispersive system). If the solute is non-dispersive, D_L = 0.0, the elution band should be close to the elution band of the reference solution, but the elution band is broadened if the solute is under the dispersive condition, D_L = 1.0. As shown in Figure 14, the elution bands of the non-dispersive solutes were perfectly matched with the corresponding elution bands in the reference solutions. In Figure 14d, the elution order of front ends were turned around. Both solutes have close shock front migration velocities by convection (two shock fronts are close in the reference solution). However, the exceptional dispersion accelerates the front-end migration velocity of the more-retained

solute, and the dispersed profile of the more-retained solute migrates faster than the shock profile of the less-retained solute.

To simulate the diverse dispersion system studied in this section with MC scheme or other numerical schemes, the large number of cells (spatial nodes) is required to describe the profile of the least dispersed solute while it is too lavish for the simulation of other more dispersed solutes. The MC-AC scheme can provide relatively good accuracy both less and more dispersed solutes.

3.6.Simulation of various isotherm shapes and multi-component systems with MC-AC scheme

The Langmuir adsorption isotherm is well-known and thermodynamically consistent. However, it is one of the simplest isotherm models in liquid chromatography, so that many empirical and theoretical isotherm models were introduced to describe complex adsorption behaviors (Guiochon et al., 1994). In this work, the generalized Langmuir model, which is commonly used for the mixed system of Langmuirian and anti-Langmuirian adsorptions by switching the sign of the Langmuir adsorption model parameters in the denominator, was also tested. As shown in Table 3, four different combinations of adsorption types, SMB-Conditions 3 to 6 were tested: Langmuirian ($p_A = p_B = 1$; Condition 3), mixed ($p_A = 1,\ \ p_B = -1$; Condition 4), mixed ($p_A = -1,\ \ p_B = 1$; Condition 5), and anti-Langmuirian ($p_A = p_B = -1$; Condition 6). Since some of b_i parameters are negative, so that the necessary condition for generalized Langmuir isotherms, Eq. (14-2) may be violated at the same feed concentration condition as the Conditions 1 and 2. Therefore, b_i parameters were one order of magnitude smaller. To obtain clear adsorption and desorption profiles of Riemann problems, fast flow-rates of the zones 1 and 3 were set compared to the Conditions 1 and 2. In this simulation work, the commercial chromatographic process simulator was unstable with generalized Langmuir isotherms (in anti-Langmuirian and mixed condisions). It seems that the anti-Langmuirian and mixed conditions occur significant *partition inconsistency* errors, i.e. the Courant numbers in the computational nodes often violate the stable condition, $0 \leq \mathcal{C}_i \leq 1$, so that the conventional discretization methods fall to

providing unstable solutions. Therefore, the proposed MC-AC scheme could not compared with the widely-established numerical methods in these conditions.

Figure 15 compared four different adsorption types, the Conditions 3 to 6. For all four different types, the MC-AC scheme could provide good solution with 50 cells compared to the reference solutions (MC scheme with 10000 cells). Since the flow-rates in zones 1 and 3 are much faster than Conditions 1 and 2, i.e. it requires more discretized time steps to compute ($\Delta t = \Delta z/u_L$), the computation time was slower than Conditions 1 and 2 (cf. Conditions 1 and 3 to 6 in Table 4). When 200 cells were involved, i.e. the cell size is small enough to provide good resolution, the solutions are perfectly matched to the reference solutions, and the computation time was approximately 800 times faster than the reference scheme (cf. Table 4).

As the number of solutes increases, the isotherm behaviors are more complex, and it is not easy to get an accurate solution because of significant *partition inconsistency* error. In the MC-AC scheme, the *partition inconsistency* error is quantified to be actively modulated. Therefore, it can provides good solutions for multi-component systems. Up to 5-component system (SMB-Conditions 7 to 9 in Table 3), the MC-AC scheme was applied to simulate the SMB process at the Condition 1, which provides complex superposed shock fronts. To apply adsorption nonlinearity similar to the Condition 1, the same total feed concentration was tested. From the binary system (the Conditions 1 and 2 in Table 1), one component (solute B in Conditions 7 to 9) that retains between the binary system solutes (solutes A and C in Conditions 7 to 9) and two more components (solutes D and E) that retain less than the solute C were add with arbitrarily decided isotherm parameters, a_i. The isotherm parameters, a_i was decided to maintain the thermodynamic consistency ($a_i/b_i = a_j/b_j$). In the quinary system (Condition 9), the selectivity of the most- and the least-retained solutes, a_A/a_E = 8. This means that widely diverse retention system in the SMB process was tested. If the selectivity is too broad, other advanced operation strategies, such as solvent-gradient SMB should be applied.

Figure 16 compared the numerical solutions from binary (Condition 1) to quinary systems with their reference solutions (MC scheme with 10000 cells). The MC-AC scheme can provide accurate solutions even though multiple components generate complex shock waves. The elution

profiles between 2 to 3 of z/L_C become more complex as the number of solutes increases. However, the MC-AC scheme with 50 cells (limited resolution) can provides good approximated profiles. Especially, the position of shock fronts were perfectly matched with the reference solutions (cf. Figure B-1 in Appendix B). To obtain the solutions similar to the reference solution accuracy (similar L^1 errors), more cells that can provide finer resolution were required as a mixture is more complex. The numerical solution with 500 cells was closely matched to the reference solution in the quinary system (cf. Conditions 1 and 7 to 9 in Table 4).

4. Conclusion

This article provides a rapid and accurate numerical method capable to solve dynamic problems occurred in chromatographic separation processes. The classical mixing cell (MC) scheme corresponds to the finite volume method (FVM) with the first-order upwind discretization scheme (UDS). It should be noted that all physicochemical phenomena could take place inside the cell with the unit volume properties and models. Due to the simplicity of the MC scheme, the numerical errors could be quantitatively evaluated. The second-order derivative term in truncation error was actively modulated to compensate the physical dispersion effect by applying the modified dispersion model with the fictitious dispersion coefficient. The addtitional *partition inconsistency* error caused by discretizing the continuous and differentiable solution section to finite volume element could be also quantified and effectively corrected. This *partition inconsistency* error is amplified if the adsorption isotherms are nonlinear and competitive. By quantifying and modulating the above-mentioned errors with the active counteraction (AC) scheme, the accuracy of the mixing cell (MC) scheme can be remarkably improved. This was proven in the simulations of challenging multi-column simulated moving bed (SMB) process for various adsorption isotherm types. It can be effectively applied for numerous other configurations of chromatographic process including control problems.

Acknowledgements

The authors cordially thank to Prof. Shamsul Qamar and Dr. Diertrich Flockerzi for their valuable comments and advices.

References

Abel, S., Mazzotti, M., & Morbidelli M. (2002). Solvent gradient operation of simulated moving beds I. Linear isotherms. *J. Chromatogr. A, 944,* 23-39.

Abel, S., Mazzotti, M., & Morbidelli M. (2002). Solvent gradient operation of simulated moving beds I. Langmuir isotherms. *J. Chromatogr. A, 1026,* 47-55.

Alhumaizi, K. (2004). Comparison of finite difference methods for the numerical simulation of reacting flow. *Comput. Chem. Eng., 28,* 1759-1769.

Amdahl, G.M. (1967). Validity of the single processor approach to achieving large scale computing capabilities. *AFIPS Conference Proceedings, 30,* 483-485.

Andrade Neto, A. S., Secchi, A. R., Souza Jr., M. B., & Barreto Jr., A. G. (2016). Nonlinear model predictive control applied to the separation of praziquantel in simulated moving bed chromatography. *J. Chromatogr. A, 1470,* 42-49.

Broughton, D. B., Neuzil, R. W., Pharis, J. M., & Brearby. C. S. (1970). The parex process for recovering paraxylene. *Chem. Eng. Prog. 66.* 70-75.

Burden, R. L. & Faires, J. D. (1993). Numerical analysis (fifth edition). Boston: PWS Publishing Company.

Courant, R., Friedrichs, K., & Lewy, H. (1928). Über die partiellen Differenzengleichungen der mathematischen Physik. Math. Ann., 100, 32-74.

Courant, R., Isaacson, E., & Rees, M. (1952). On the solution of nonlinear hyperbolic differential equations by finite differences. *Commun. Pure Appl. Math., 5,* 243-255.

Črnjaric-Žić, N., Vuković, S., & Sopta, L. (2004). Balanced finite volume WENO and central WENO schemes for the shallow water and the open-channel flow equations. J. Comput. Phys., 200, 512-548.

Craig, L. C. (1944). Identification of small amounts of organic compounds by distribution studies: II. Separation by counter-current distribution. *J. Biol. Chem., 155,* 519-534.

Czok, M. & Guiochon, G. (1990a). The physical sense of simulation models of liquid hromatography: propagation through a grid or solution of the mass balance equation. *Anal. Chem., 62,* 189-200.

Czok, M. & Guiochon, G. (1990b). Comparison of the results obtained with different models for the simulation of preparative chromatography. *Comput. Chem. Eng., 14,* 1435-1443.

DeVault, D. (1943). The theory of chromatography. *J. Am. Chem. Soc., 65,* 532-540.

Coimbra, M. C., Sereno, C., & Rodrigues, A. (2000). Modelling multicomponent adsorption process by a moving finite element method. *J. Comput. App. Math., 115,* 169-179.

Guiochon, G., Shirazi, S. G., & Katti, A. M. (1994). Fundamentals of preparative and nonlinear chromatography. Boston: Academic Press.

Heuer, C., Seidel-Morgenstern, A., & Hugo, P. (1995). Experimental investigation and modelling of closed-loop recycling in preparative chromatography. *Chem. Eng. Sci., 50,* 1115-1127.

Jiang, G.S. & Shu, C.-W. (1996). Efficient implementation of weighted ENO scheme. *J. Comput. Phys.*, *126*, 202-228.

John, V. & Novo, J. (2012). On (essentially) non-oscillatory discretizations of evolutionary convection-diffusion equations. *J. Comput. Phys.*, *231*, 1570-1586.

Kim, K.-M., Lee, J. W., Kim, S., Santos da Silva, F. V., Seidel-Morgenstern, A., & Lee, C.-H. (2017). Advanced operating strategies to extend the applications of simulated moving bed chromatography. *Chem. Eng. Technol.*, *40*, 2163-2178.

Klatt, K. U., Hanisch, F., & Dünnebier, G. (2002). Model-based control of a simulated moving bed chromatographic process for the separation of fructose and glucose. *J. Process Control*, *12*, 203-219.

Kramers, H. & Alberda, G. (1953). Frequency response analysis of continuous flow systems. Chem. Eng. Sci., 2, 173-181.

Lax, P. D. & Wendroff, B. (1960). Systems of conservation laws. *Commun. Pure Appl. Math.*, *13*, 217-237.

Leão, C. P. & Rodrigues, A. E. (2004). Transient and steady-state models for simulated moving bed processes: numerical solutions. *Comput. Chem. Eng.*, *28*, 1725-1741.

Lee, J. W., Horáth, Z., O'Brien, A. G., Seeberger, P. H., & Seidel-Morgenstern, A. (2014). Design and optimization of coupling a continuously operated reactor with simulated moving bed chromatography. *Chem. Eng. J.*, *251*, 355–370.

Lee, J. W., & Seidel-Morgenstern, A. (2018). Model predictive control of simulated moving bed chromatography for binary and pseudo-binary separations: simulation study. *IFAC PapersOnLine*, *51*, 530-535.

LeVeque, R. J. (2002). Finite volume methods for hyperbolic problems. New York: Cambridge University Press.

LeVeque, R. J. (2007). Finite difference methods for ordinary and partial differential equations: steady-state and time-dependent problems. Philadelphia: SIAM.

Liu, X.-D., Osher, S., & Chan, T., (1994). Weighted essentially non-oscillatory schemes. *J. Comput. Phys.*, *115*, 200-212.

Martin, A. J. P., Synge, R. L. M. (1941). A new form of chromatogram employing two liquid phases. *Biochem. J.*, *35*, 1358-1368.

Mazzotti, M. (2006). Equilibrium theory based design of simulated moving bed processes for a generalized Langmuir isotherm. *J. Chromatogr. A, 1126*, 311-322.

Migliorini, C., Gentilini, A., Mazzotti, M., & Morbidelli, M. (1999). Design of simulated moving bed units under nonlinear conditions *Ind. Eng. Chem. Res.*, *38*, 2400-2410.

Rhee, H.-K., Aris, R, & Amundson N. R. (1989). First-order partial differential equations: volume 2 theory and application of hyperbolic systems of quasilinear equations. Mineola: Dover Publications.

Rouchon, P., Schonauer, M., Valentin, P., & Guiochon, G. (1987). Numerical simulation of band propagation in nonlinear chromatography. *Sep. Sci. Technol.*, *22*, 1793-1883.

Roureiro, M. & Rodrigues, A. E. (1991). Two solution methods for hyperbolic systems of partial differential equations in chemical engineering. *Chem. Eng. Sci.*, *46*, 3259-3267.

Storti, G., Mazzotti, M., Morbidelli, M., & Carrà, S. (1993). Robust design of binary countercurrent adsorption separation processes. *AIChE J.*, 39, 471-492.

Villermaux, J. (1987). Chemical engineering approach to dynamic modelling of linear chromatography: A flexible method for representing complex phenomena from simple concempts. *J. Chromatogr.*, *406*, 11-26.

von Lieres, E. & Andersson, J. (2010). A fast and accurate solver for the general rate model of column liquid chromatography. *Comput. Chem. Eng.*, *34*, 1180-1191.

Wu, D.-J., Xie, Y., Ma, Z., & Wang, N.-H. L. (1998). Design of simulated moving bed chromatography for amino acid separations. *Ind. Eng. Chem. Res.*, *37*, 4023-4035.

Zhong, G., & Guiochon, G. (1996). Analytical solution for the linear ideal model of simulated moving bed chromatography. *Chem. Eng. Sci.*, *51*, 4307-4319.

List of Tables

List of Figures

Figure 4. Schematic structure of computation routines of the MC-AC scheme.

Figure 5. Comparisons of the internal concentration profiles obtained by the MC scheme.
a) Condition 1; b) Condition 2;
At the end of 20th cycle operation, $D_{L,i}$ = 0;
Reference solutions: #$\mathbf{N}_C$ = 10000.

Figure 6. Comparisons of the internal concentration profiles obtained by the MC-AC scheme and the reference solution.
a) #$\mathbf{N}_C$ = 20, Condition 1; b) #$\mathbf{N}_C$ = 20, Condition 2;
c) #$\mathbf{N}_C$ = 200, Condition 1; d) #$\mathbf{N}_C$ = 200, Condition 2;
Cell concentration profiles; at the end of 20th cycle operation; $D_{L,i}$ = 0.

Figure 7. Comparisons of the characteristic hodograph lines of the reference and MC-AC solutions.
a) #$\mathbf{N}_C$ = 20, Condition 1; b) #$\mathbf{N}_C$ = 20, Condition 2;
c) #$\mathbf{N}_C$ = 200, Condition 1; d) #$\mathbf{N}_C$ = 200, Condition 2;
At the end of 20th cycle operation; $D_{L,i}$ = 0.

Figure 8. Comparisons of the MC and MC-AC schemes in terms of computation time (a) and the parallel computation efficiency (b).

Figure 9. Comparisons of the internal concentration profiles obtained with various numerical methods.
a) UDS; b) BUDS; c) OSPRE; d) MC-AC;
Interpolated concentration profiles; Condition 1; at the end of 20th cycle operation; $D_{L,i}$ = 0.

Figure 10. The internal concentration profile variations by the number of cells in MC-AC and OSPRE.
a) MC-AC, Condition 1; b) MC-AC, Condition 2;
c) OSPRE, Condition 1; d) OSPRE, Condition 2;
Interpolated concentration profiles; at the end of 20th cycle operation; $D_{L,i}$ = 0.

Figure 11. Comparisons of the MC-AC and OSPRE schemes in terms of L^1 (a) and L^∞ (b) errors.

Figure 12. Comparisons of the MC-AC and OSPRE schemes in terms of computation speed and L^1 error
Conditions 1 and 2; at the end of 20th cycle operation; $D_{L,i}$ = 0.

Figure 13. The internal concentration profile variations by the number of cells in MC-AC scheme with the fixed physical dispersion coefficients.
a) $D_{L,A}$; $D_{L,B}$ = 0.1;0.1, Condition 1; b) $D_{L,A}$; $D_{L,B}$ = 0.1;0.1, Condition 2;
c) $D_{L,A}$; $D_{L,B}$ = 1.0;1.0, Condition 2; d) $D_{L,A}$; $D_{L,B}$ = 1.0;1.0, Condition 2;
Interpolated concentration profiles; at the end of 20th cycle operation.

Figure 14. The internal concentration profile variations in the diverse physical dispersion systems using MC-AC scheme.
a) $D_{L,A}$; $D_{L,B}$ = 0.0;1.0, Condition 1; b) $D_{L,A}$; $D_{L,B}$ = 1.0;0.0, Condition 1;
c) $D_{L,A}$; $D_{L,B}$ = 0.0;1.0, Condition 2; d) $D_{L,A}$; $D_{L,B}$ = 1.0;0.0, Condition 2;
Interpolated concentration profiles; at the end of 20th cycle operation.

Figure 15. Comparisons of the reference and numerical solutions obtained by MC-AC scheme in various isotherm types.
a) Condition 3 (Langmuirian); b) Condition 4 (Mixed);

c) Condition 5 (Mixed); d) Condition 6 (anti-Langmuirian);
Interpolated concentration profiles; at the end of 20th cycle operation; $D_{L,i}$ = 0.

Figure 16. Comparisons of the internal concentration profiles obtained up to five-component mixtures.
a) Condition 1 (Binary); b) Condition 7 (Ternary);
c) Condition 8 (Quaternary); d) Condition 9 (Quinary);
Interpolated concentration profiles; at the end of 20th cycle operation; $D_{L,i}$ = 0.

Appendix A

To illustrate the computational complexity of physically meaningful partition parameters, let us consider binary system (solutes A and B) that causes rarefaction and shock waves (Figure A-1). If all cell concentrations are well posed on the characteristic lines on the hodograph plane, cf. Eqs. (24) and (25), the locally constant partition parameters obtained from Eq. (8-2) are physically meaningful. On the other hand, the physically meaningful representative values should be obtained. The one possible way is using the following weighted averages in a rarefaction wave condition,

$$\bar{\kappa}_i^{rw} = 1 + \frac{F}{\Delta t}\left\{\Delta t^{rw}\frac{\bar{q}_i^{rw}(n,t+\Delta t^{rw})-\bar{q}_i(n,t)}{\bar{c}_i^{rw}(n,t+\Delta t^{rw})-\bar{c}_i(n,t)} + (\Delta t-\Delta t^{rw})\frac{\bar{q}_i(n,t+\Delta t)-\bar{q}_i^{rw}(n,t+\Delta t^{rw})}{\bar{c}_i(n,t+\Delta t)-\bar{c}_i^{rw}(n,t+\Delta t^{rw})}\right\} \quad \text{(A-1)}$$

and in a shock wave condition,

$$\bar{\kappa}_i^{sw} = 1 + \frac{F}{\Delta t}\left\{\Delta t^{sw}\frac{\bar{q}_i^{sw}(n,t+\Delta t^{sw})-\bar{q}_i(n,t)}{\bar{c}_i^{sw}(n,t+\Delta t^{sw})-\bar{c}_i(n,t)} + (\Delta t-\Delta t^{sw})\frac{\bar{q}_i(n,t+\Delta t)-\bar{q}_i^{sw}(n,t+\Delta t^{sw})}{\bar{c}_i(n,t+\Delta t)-\bar{c}_i^{sw}(n,t+\Delta t^{sw})}\right\} \quad \text{(A-2)}$$

where the superscripts, rw and sw denote the rarefaction and shock wave conditions, respectively.

The characteristic hodograph directions at the point, $(\bar{c}_1, \bar{c}_2, \dots, \bar{c}_{N_S})$can be obtained using the following system of equations (Rhee et al., 1989),

$$\frac{\mathcal{D}\bar{q}_1}{\mathcal{D}\bar{c}_1} = \frac{\mathcal{D}\bar{q}_2}{\mathcal{D}\bar{c}_2} = \cdots = \frac{\mathcal{D}\bar{q}_{N_S}}{\mathcal{D}\bar{c}_{N_S}} \quad \text{(A-3)}$$

These equations provides $\#\mathbf{N}_S$ directions for a certain hodograph point, so that $(\#\mathbf{N}_S)!$ possible trajectories should be considered. Applying the entropy conditions correspondent to the physical system, which is related to the elution order of solutes in adsorption, one correct wave trajectory should be chosen.

For example, two transient concentration points, $(\bar{c}_A^{sw}, \bar{c}_B^{sw})$ and $(\bar{c}_A^{rw}, \bar{c}_B^{rw})$ should be obtained in binary mixture as shown in Figure A-1, and the corresponding transient concentration point should be chosen for a rarefaction or shock wave trajectories, respectively.

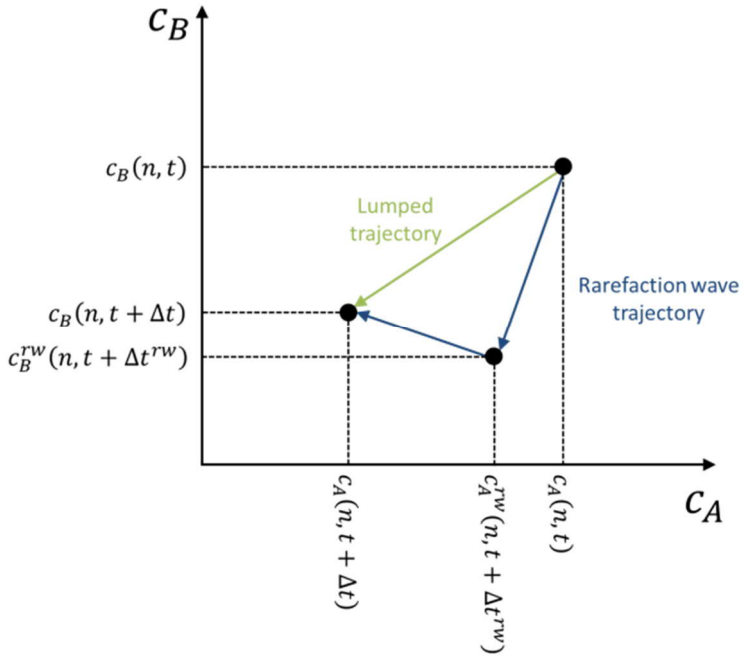

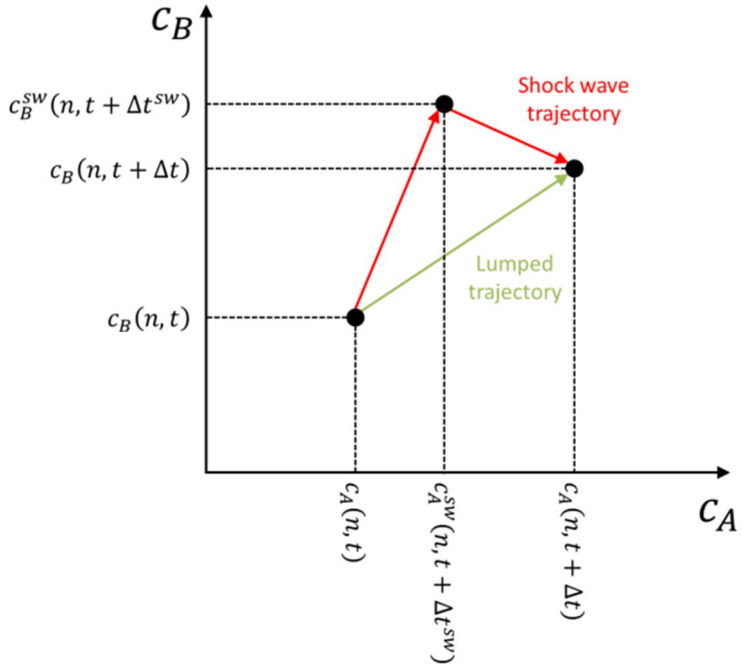

Figure A-1. Schematic hodograph illustrations of rarefaction (upper) and shock (lower) waves in binary mixture system (solutes A and B, competitive Langmuir isotherms, and solute A is more-retained).

Appendix B

In the chosen commercial simulator, Aspen Chromatography® (and most of commercial PDE solvers for the hyperbolic conservation laws), the PDEs are transformed to the DAEs by taking discretized fluxes as,

$$\frac{d\bar{c}_i(n,t)}{dt} = \alpha_{i,n}\left\{\mathcal{F}_i\left(n-\tfrac{1}{2},t\right) - \mathcal{F}_i\left(n+\tfrac{1}{2},t\right)\right\} \tag{B-1}$$

where $\mathcal{F}_i\left(n-\frac{1}{2},t\right)$ and $\mathcal{F}_i\left(n+\frac{1}{2},t\right)$ are the entering and leaving fluxes of the n^{th} spatial node at time t, $\alpha_{i,n}$ is the system parameter. The fluxes can be expressed as a linear combination of concentrations using a proper numerical scheme.

$$\begin{pmatrix} \frac{d\bar{c}_1(1,t)}{dt} \\ \vdots \\ \frac{d\bar{c}_{N_S}(N_C,t)}{dt} \end{pmatrix} = \boldsymbol{\mathcal{A}} \cdot \begin{pmatrix} \bar{c}_1(1,t) \\ \vdots \\ \bar{c}_{N_S}(N_C,t) \end{pmatrix} \tag{B-2}$$

where $\boldsymbol{\mathcal{A}}$ is the square matrix that contains the system parameters and adsorption isotherms. The sparsity of matrix $\boldsymbol{\mathcal{A}}$ is depends on the chosen numerical scheme. For example, the OSPRE scheme take three spatial nodes, $n-1$, n, and $n+1$. Therefore, the matrix $\boldsymbol{\mathcal{A}}$ is $(\#\mathbf{N}_S \cdot \#\mathbf{N}_C)$-by-$(\#\mathbf{N}_S \cdot \#\mathbf{N}_C)$ tri-diagonal matrix. To simplify the computation, it is assumed that the fluxes are locally constant, i.e. the matrix $\boldsymbol{\mathcal{A}}$ is constant. Therefore, Eq. (B-2) is not identical to,

$$\begin{pmatrix} \frac{d\kappa_1(1,t)\bar{c}_1(1,t)}{dt} \\ \vdots \\ \frac{d\kappa_{N_S}(N_C,t)\bar{c}_{N_S}(N_C,t)}{dt} \end{pmatrix} = \boldsymbol{\mathcal{B}} \cdot \begin{pmatrix} \bar{c}_1(1,t) \\ \vdots \\ \bar{c}_{N_S}(N_C,t) \end{pmatrix} \tag{B-3}$$

where $\boldsymbol{\mathcal{B}}$ is the square matrix that contains the system parameters. It causes the *partition inconsistency* error, which increases where the isotherms are nonlinear and competitive. Figure B-1 shows the examples for binary linear isotherms and quinary Langmuir isotherms. The solutions obtained using the MC-AC and OSPRE schemes were compared. In linear isotherms, adsorption of each components are not nonlinear nor competitive, so that there is no inconsistency (the positions of front and rear ends are located at the same positions of the reference solutions as shown in Figures B-1a and B-1c). However, in Langmuir isotherms, competitive nonlinear isotherms, significant inconsistency arose

during the discretized numerical approximation, and causes inaccurate migration velocity. As shown in Figures B-1d, the shock wave positions were deviated in the OSPRE scheme if small number of spatial nodes were used $\#\mathbf{N}_C$ = 50). The shock front of solute C is located in the middle of total elution band (the position of shock wave is affected by all other solutes), so that its position was significantly deviated compared to other shock waves. These *partition inconsistency* errors can be minimized by using dense spatial nodes that requires enormous computation resources, e.g. the computed profiles with $\#\mathbf{N}_C$ = 500 were closely matched to the reference solution, but its computation time was 135 times longer than $\#\mathbf{N}_C$ = 50. On the other hand, the MC-AC scheme eliminates quantified *partition inconsistency* error, so that the position of the shock waves are identical in both $\#\mathbf{N}_C$ = 50 and $\#\mathbf{N}_C$ = 500 profiles.

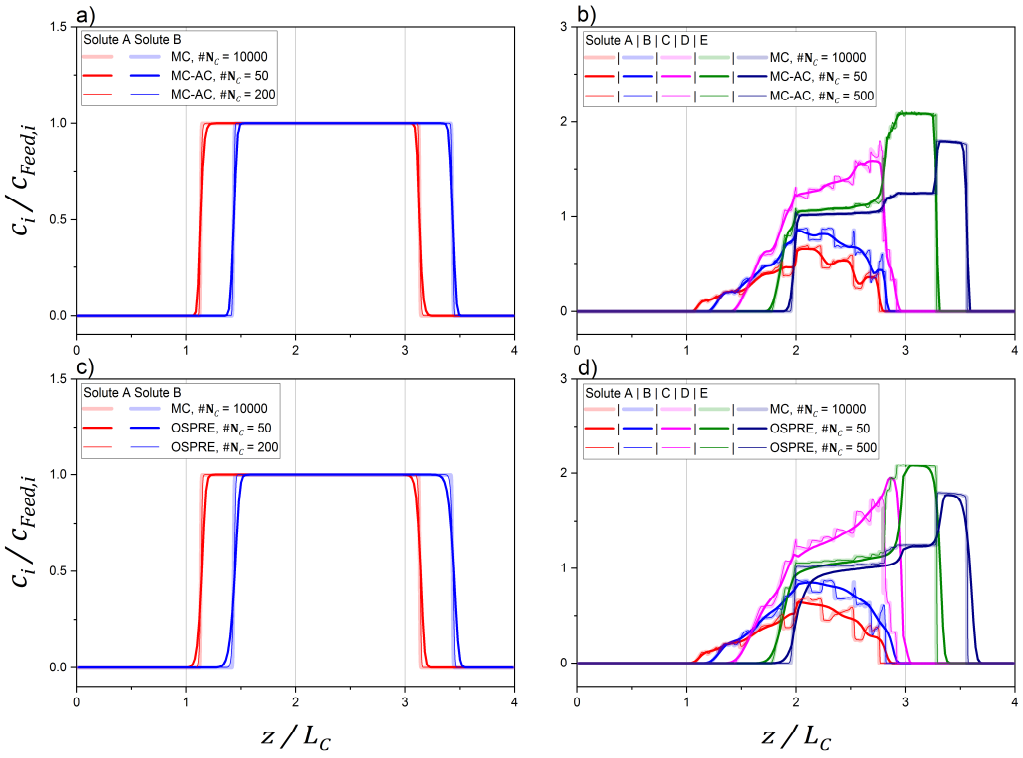

Figure B-1. Numerical scheme comparisons of internal concentration profiles obtained from binary mixture and linear isotherms system and quinary mixture and Langmuir isotherms system.

a) MC-AC scheme, Linear system; b) MC-AC scheme, Condition 9;

c) OSPRE scheme, Linear system; d) OSPRE scheme, Condition 9;

Linear system: H_A = 4, H_B = 2, Q_{Z1} to Q_{Z4} = 30, 10, 30, 10 ml/min

Interpolated concentration profiles, at the end of 20th cycle operation, $D_{L,i}$ = 0.

Figure B-2 compares the characteristic hodograph lines obtained from the reference and OSPRE solutions (cf. Figure 8). In low-resolution conditions, $\#\mathbf{N}_C$ = 20, the OSPRE solutions imply significant numerical errors, the *partition inconsistency* and *numerical dispersion* errors. The characteristic lines are deviated from the reference solutions when complex shock waves amplify the *partition inconsistency* error (Figure B-2a), and the nodes involved to describe the steep-and-narrow shock wave are not sufficient to eliminate the *numerical dispersion* error (Figure B-2b). These errors can be minimized by increasing the number of nodes, $\#\mathbf{N}_C$ = 200 in Figures B-2c and B-2d.

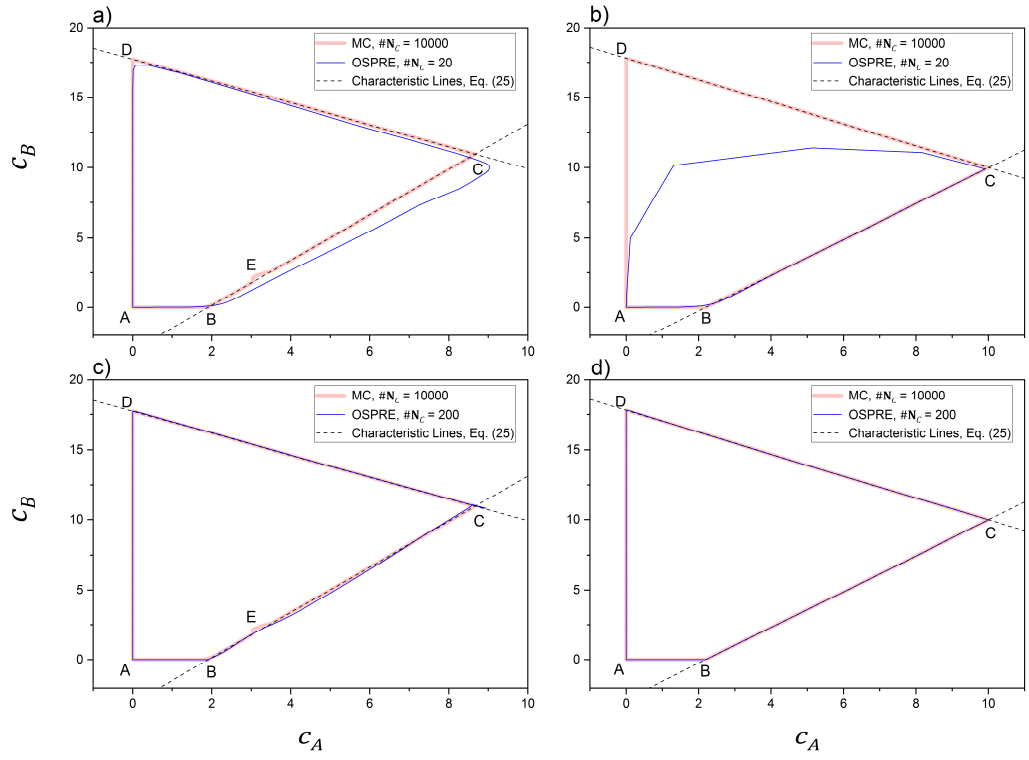

Figure B-2. Comparisons of the characteristic hodograph lines of the reference and OSPRE solutions.

a) $\#\mathbf{N}_C$ = 20, Condition 1; b) $\#\mathbf{N}_C$ = 20, Condition 2;

c) $\#\mathbf{N}_C$ = 200, Condition 1; d) $\#\mathbf{N}_C$ = 200, Condition 2;

At the end of 20th cycle operation, $D_{L,i}$ = 0, cf. Figure 8.

Table 1

SMB-Condition	Operating Conditions[1)]		Isotherms, $\boldsymbol{a_i}$ [-]; $\boldsymbol{p_i b_i}$ [L/g]	
	$c_{Feed,i}$[2)] [g/L]	Q_{Z1} to Q_{Z4} [ml/min]	A	B
1	10	27; 9; 12; 9	4.0; 0.2	2.0; 0.1
2	10	27; 9; 18; 6		

[1)] Port switching interval, t_S = 4 min

[2)] The same concentration for all solutes, i = A, B

Table 2

	$\#\mathbf{N}_C$	$N_{\Delta t}$ [1]	$D_{L,i}$ = 0.0			$D_{L,i}$ = 0.1			$D_{L,i}$ = 1.0		
			$R_{\Delta t}$ [2]	$\bar{N}_{NL}$ [3]	s/cycle [4]	$R_{\Delta t}$ [2]	$\bar{N}_{NL}$ [3]	s/cycle [4]	$R_{\Delta t}$ [2]	$\bar{N}_{NL}$ [3]	s/cycle [4]
Condition 1	10	1680	1.00	19.4	0.008	1.00	19.4	0.008	1.13	9.92	0.008
	20	3360	1.00	19.4	0.029	1.00	19.4	0.029	1.67	7.43	0.029
	50	7920	1.00	20.1	0.122	1.00	11.7	0.113	4.42	6.12	0.142
	100	15780	1.00	20.7	0.491	1.14	10.8	0.467	9.30	5.66	0.590
	200	31260	1.00	21.7	1.689	1.74	8.39	1.397	19.6	5.36	2.742
	500	78180	1.00	27.3	8.602	4.48	7.63	8.630	50.2	5.02	26.55
Condition 2	10	1740	1.00	16.5	0.008	1.00	16.6	0.008	1.18	7.71	0.008
	20	3300	1.00	17.1	0.026	1.00	17.1	0.022	1.97	6.74	0.030
	50	7920	1.00	17.5	0.109	1.02	14.8	0.114	4.51	5.53	0.135
	100	15720	1.00	17.8	0.431	1.24	8.64	0.383	9.46	5.16	0.556
	200	31320	1.00	18.0	1.593	2.00	7.77	1.420	19.7	4.88	2.652
	500	78180	1.00	21.0	7.743	4.57	7.01	8.605	50.2	4.64	25.99

[1] Number of discretized time computation for convection

[2] $R_{\Delta t} = \frac{\{\text{Number of discretized time computation for error correction}\}}{\{\text{Number of discretized time computation for convection}\}}$

[3] Average iteration number of the nonlinear solver

[4] Computation speed, 1 cycle = 1 port switching interval

Table 3

SMB-Condition	Operating Conditions[1)]		Isotherms, $\boldsymbol{a_i}$ [-]; $\boldsymbol{p_i b_i}$ [L/g]				
	$c_{Feed,i}$[2)] [g/L]	Q_{Z1} to Q_{Z4} [ml/min]	A	B	C	D	E
3	10	50; 10; 50; 10	4.0; 0.02	2.0; 0.01	--	--	--
4	10	50; 10; 50; 10	4.0; 0.02	2.0; −0.01	--	--	--
5	10	50; 10; 50; 10	4.0; −0.02	2.0; 0.01	--	--	--
6	10	50; 10; 50; 10	4.0; −0.02	2.0; −0.01	--	--	--
7	7	27; 9; 12; 9	4.0; 0.2	3.0; 0.15	2.0; 0.1	--	--
8	5	27; 9; 12; 9	4.0; 0.2	3.0; 0.15	2.0; 0.1	1.0; 0.05	--
9	4	27; 9; 12; 9	4.0; 0.2	3.0; 0.15	2.0; 0.1	1.0; 0.05	0.5; 0.025

[1)] Port switching interval, t_S = 4 min

[2)] The same concentration for all solutes

Table 4

Condition	$\boldsymbol{p_A}$	$\boldsymbol{p_B}$	$\#\mathbf{N_C}$	s/cycle[1)]	Speed-up[2)]	Errors		$\#\mathbf{N_C}$	s/cycle[1)]	Speed-up[2)]	Errors	
						L^1	L^∞				L^1	L^∞
3	1	1	50	0.209	13786	6.01e-3	0.477	200	3.448	834	1.25e-3	0.417
4	1	−1	50	0.211	13245	7.69e-3	0.508	200	3.439	812	1.00e-3	0.325
5	−1	1	50	0.220	12509	6.19e-3	0.427	200	3.437	802	1.07e-3	0.333
6	−1	−1	50	0.208	14842	7.15e-3	0.416	200	3.616	855	1.71e-3	0.605
Condition	$\#\mathbf{N}_S$		$\#\mathbf{N_C}$	s/cycle[1)]	Speed-up[2)]	Errors		$\#\mathbf{N_C}$	s/cycle[1)]	Speed-up[2)]	Errors	
						L^1	L^∞				L^1	L^∞
1	2		50	0.122	11339	6.94e-3	0.331	200	1.689	818	1.48e-3	0.422
7	3		50	0.308	11454	7.04e-3	0.702	300	9.299	380	1.13e-3	0.514
8	4		50	0.383	12662	9.80e-3	0.989	400	20.81	233	1.57e-3	0.952
9	5		50	0.698	12448	1.31e-2	0.496	500	51.60	168	1.98e-3	0.455

[1)] Computation speed, 1 cycle = 1 port switching interval

[1)] Computation speed ratio to the reference solution (MC scheme, $\#\mathbf{N}_C$ = 10000)

Figure 1.

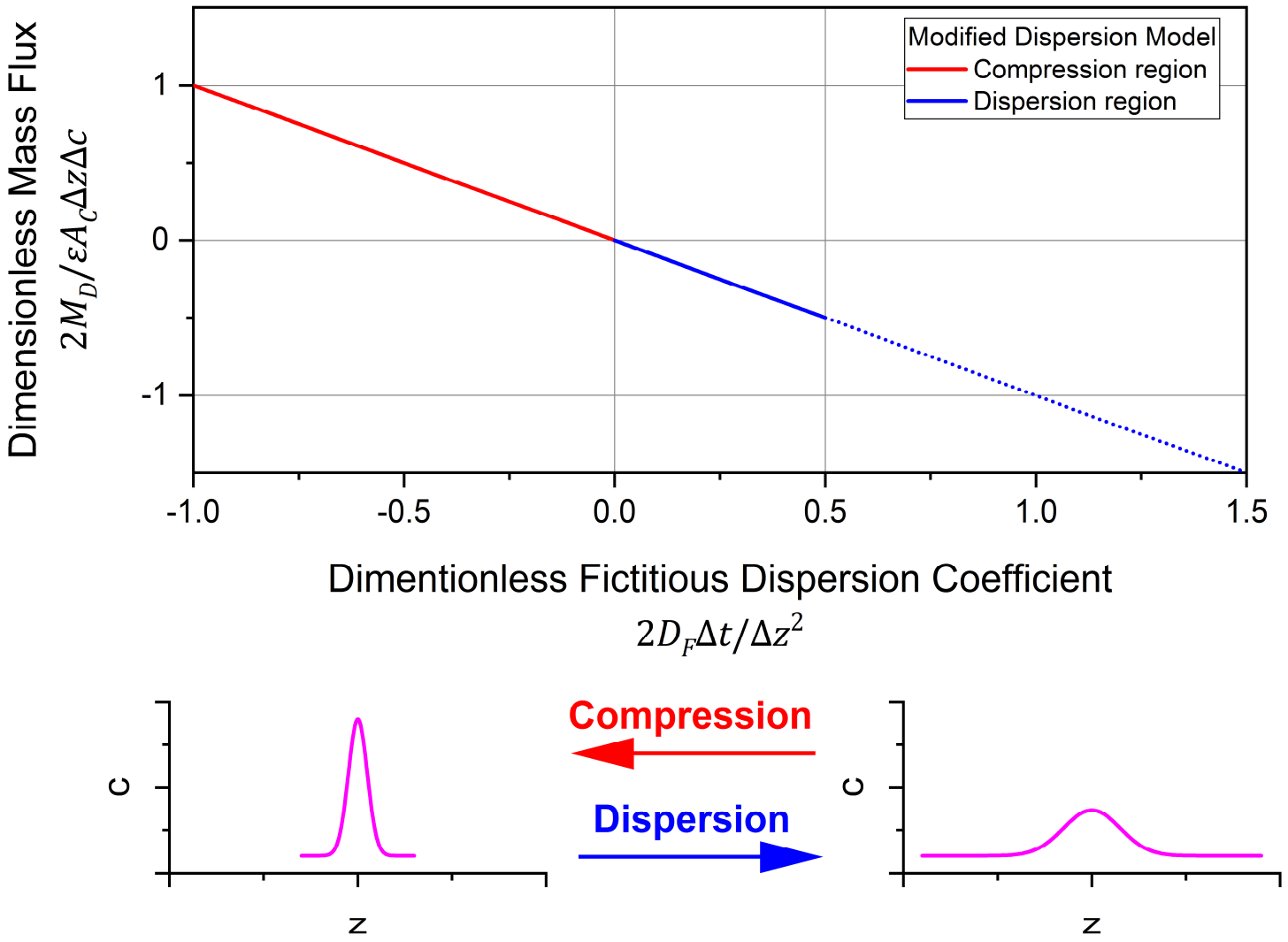
Modified Dispersion Model
Compression region
Dispersion region
Dimensionless Mass Flux
$2M_D/\varepsilon A_c \Delta z \Delta c$
1
0
-1
-1.0
-0.5
0.0
0.5
1.0
1.5
Dimentionless Fictitious Dispersion Coefficient
$2D_F \Delta t/\Delta z^2$
Compression
Dispersion
c
z
c
z

Figure 2.

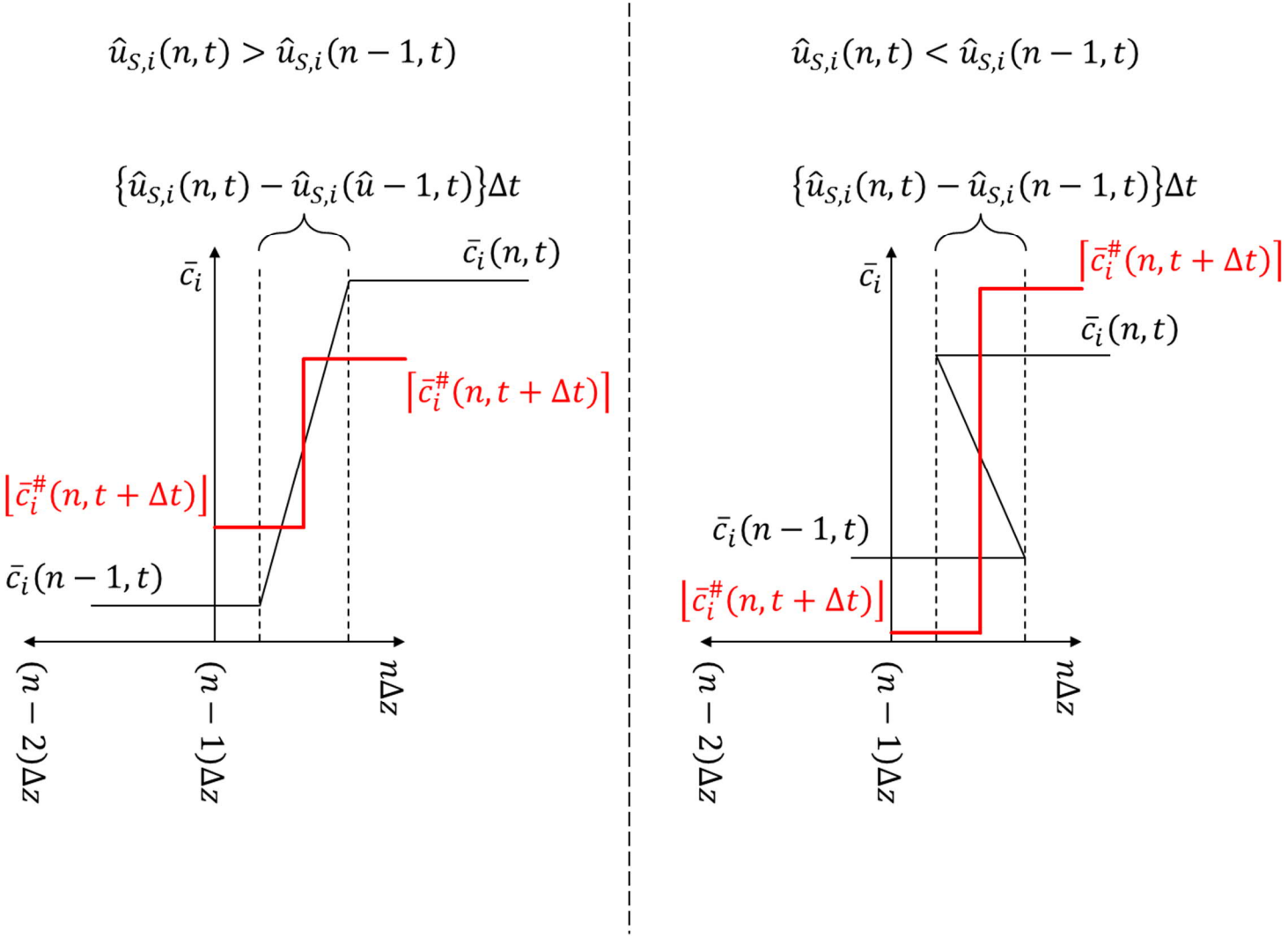
$\hat{u}_{S,i}(n,t) > \hat{u}_{S,i}(n-1,t)$
$\{\hat{u}_{S,i}(n,t) - \hat{u}_{S,i}(\hat{u}-1,t)\}\Delta t$
$\bar{c}_i$
$\bar{c}_i(n,t)$
$\lceil \bar{c}_i^{\#}(n,t+\Delta t) \rceil$
$\lfloor \bar{c}_i^{\#}(n,t+\Delta t) \rfloor$
$\bar{c}_i(n-1,t)$
$(n-2)\Delta z$
$(n-1)\Delta z$
$n\Delta z$
$\hat{u}_{S,i}(n,t) < \hat{u}_{S,i}(n-1,t)$
$\{\hat{u}_{S,i}(n,t) - \hat{u}_{S,i}(n-1,t)\}\Delta t$
$\bar{c}_i$
$\lceil \bar{c}_i^{\#}(n,t+\Delta t) \rceil$
$\bar{c}_i(n,t)$
$\bar{c}_i(n-1,t)$
$\lfloor \bar{c}_i^{\#}(n,t+\Delta t) \rfloor$
$(n-2)\Delta z$
$(n-1)\Delta z$
$n\Delta z$

Figure 3.

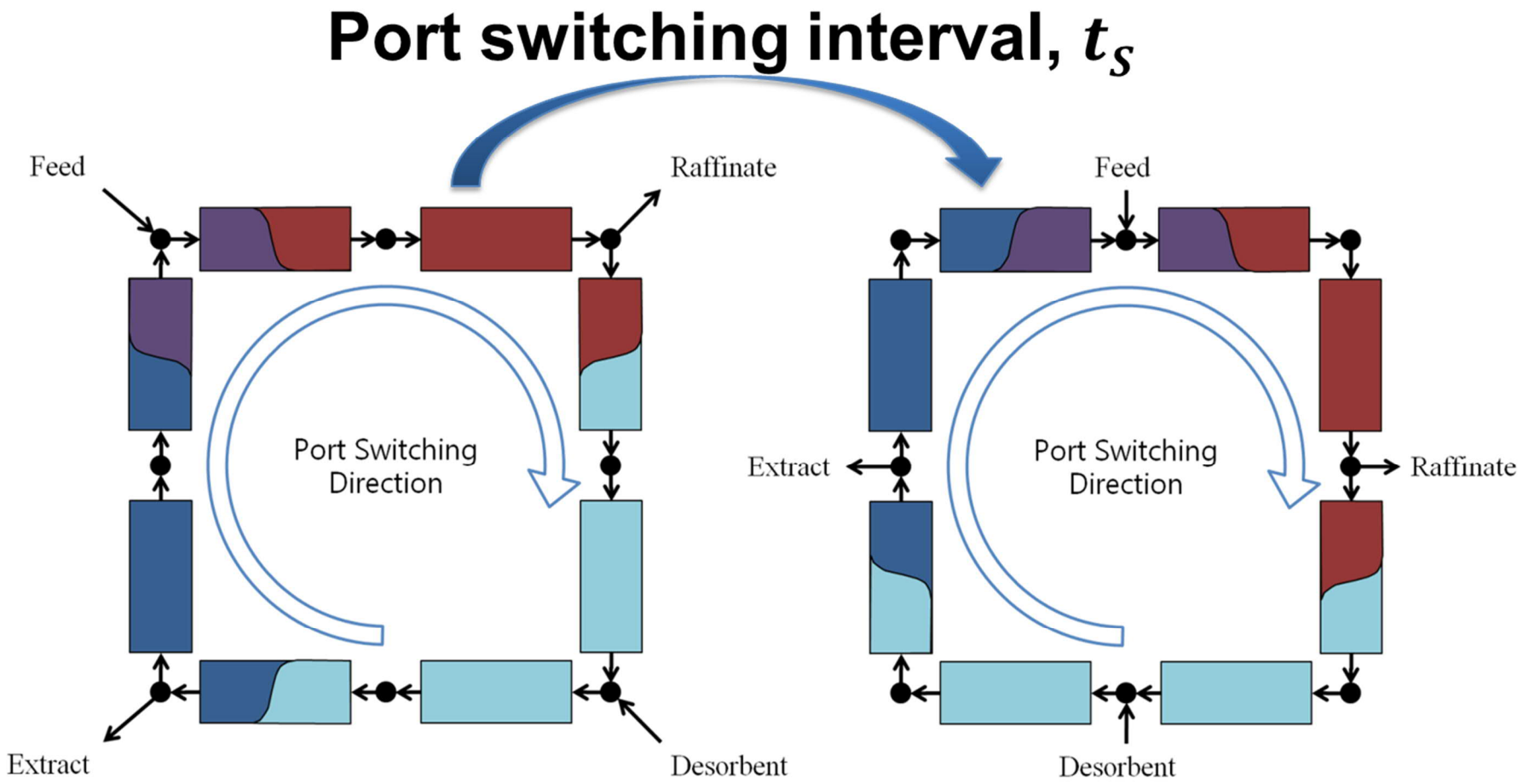
Port switching interval, t_s
Feed
Raffinate
Port Switching Direction
Extract
Desorbent
Feed
Extract
Port Switching Direction
Raffinate
Desorbent

Figure 4.

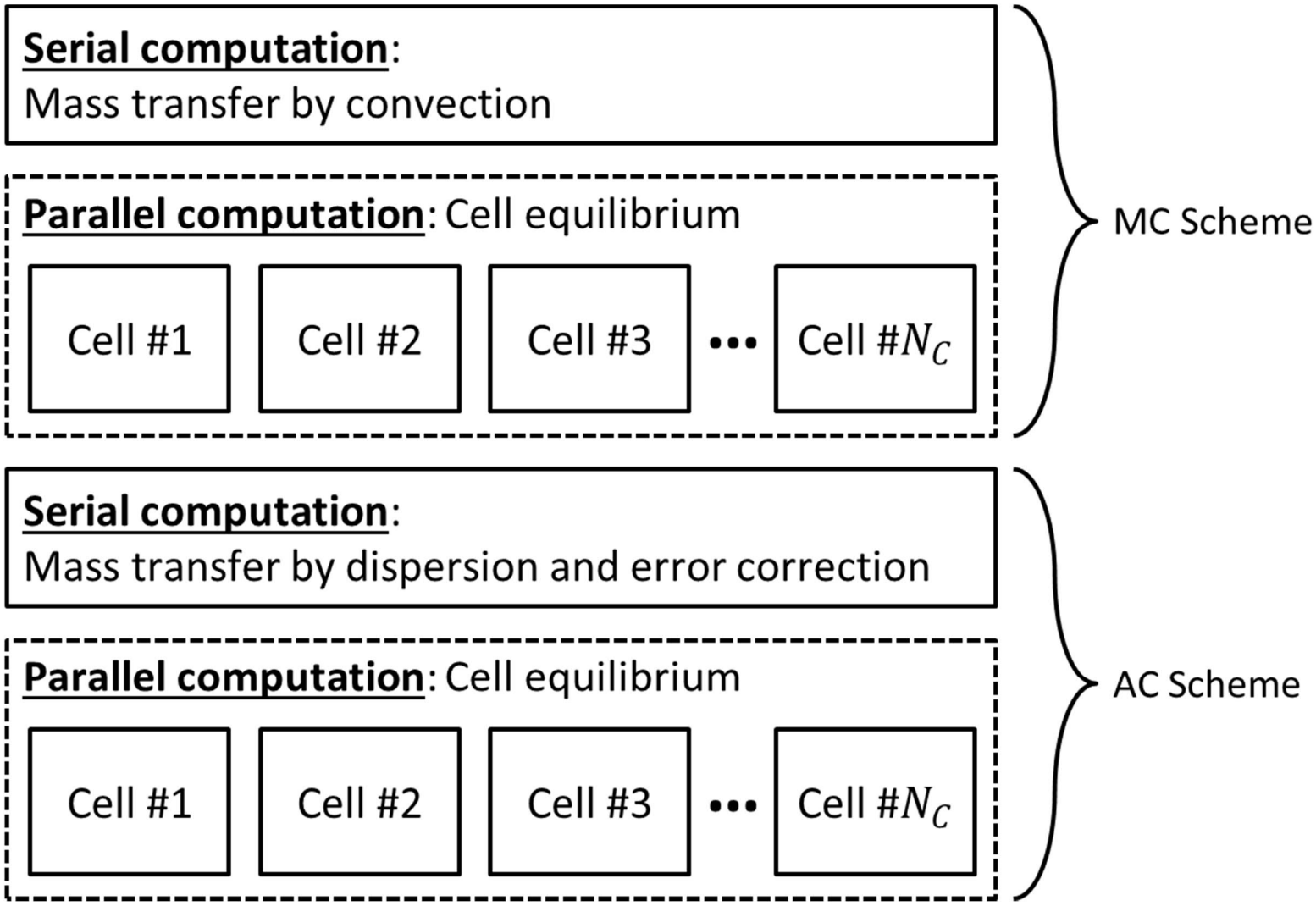
Serial computation:
Mass transfer by convection
Parallel computation: Cell equilibrium
Cell #1
Cell #2
Cell #3
Cell #N_C
MC Scheme
Serial computation:
Mass transfer by dispersion and error correction
Parallel computation: Cell equilibrium
Cell #1
Cell #2
Cell #3
Cell #N_C
AC Scheme

Figure 5.

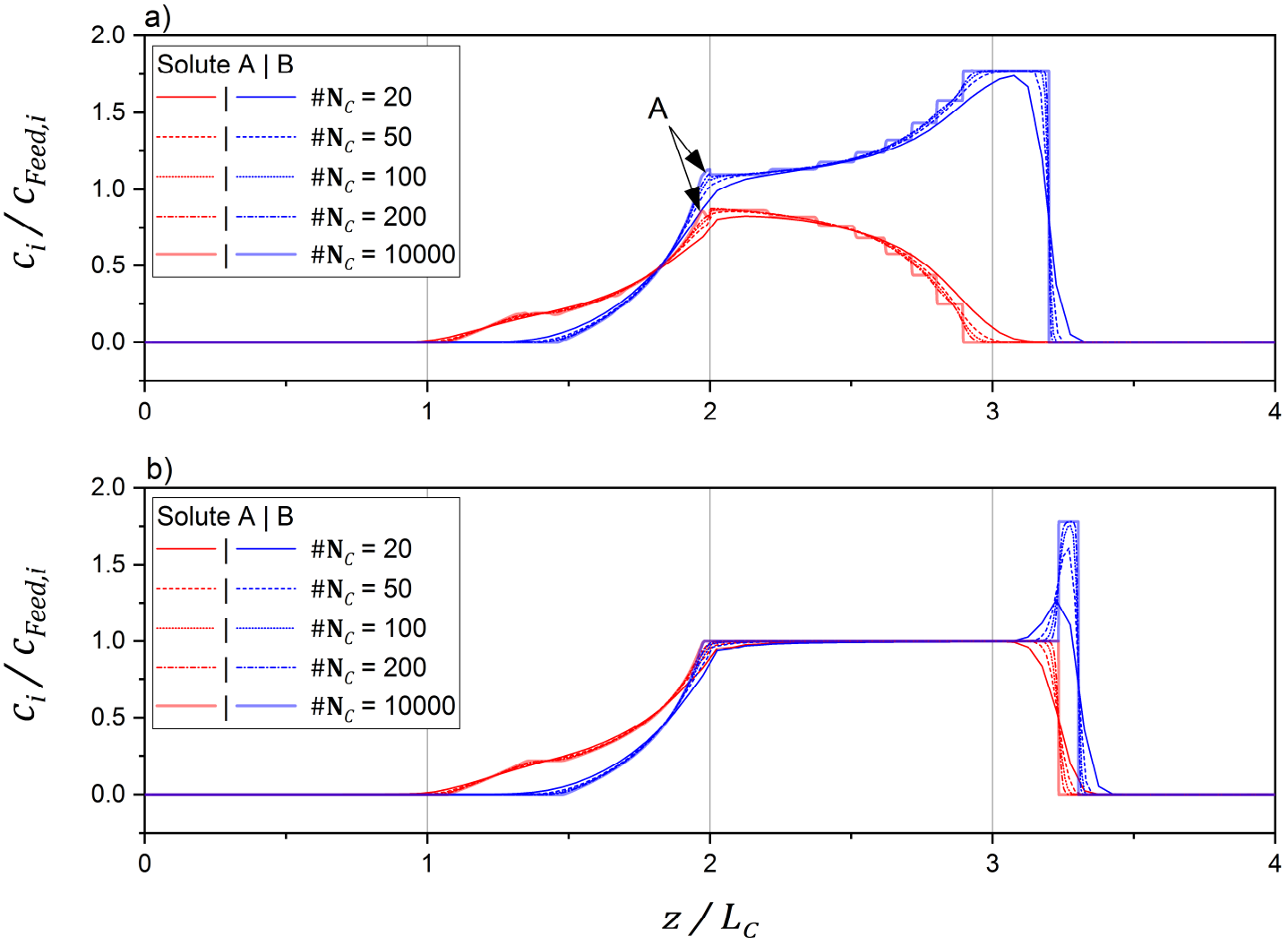
a)
b)
Solute A | B
#N_C = 20
#N_C = 50
#N_C = 100
#N_C = 200
#N_C = 10000
A
c_i / c_Feed,i
z / L_C
0.0
0.5
1.0
1.5
2.0
0
1
2
3
4

Figure 6.

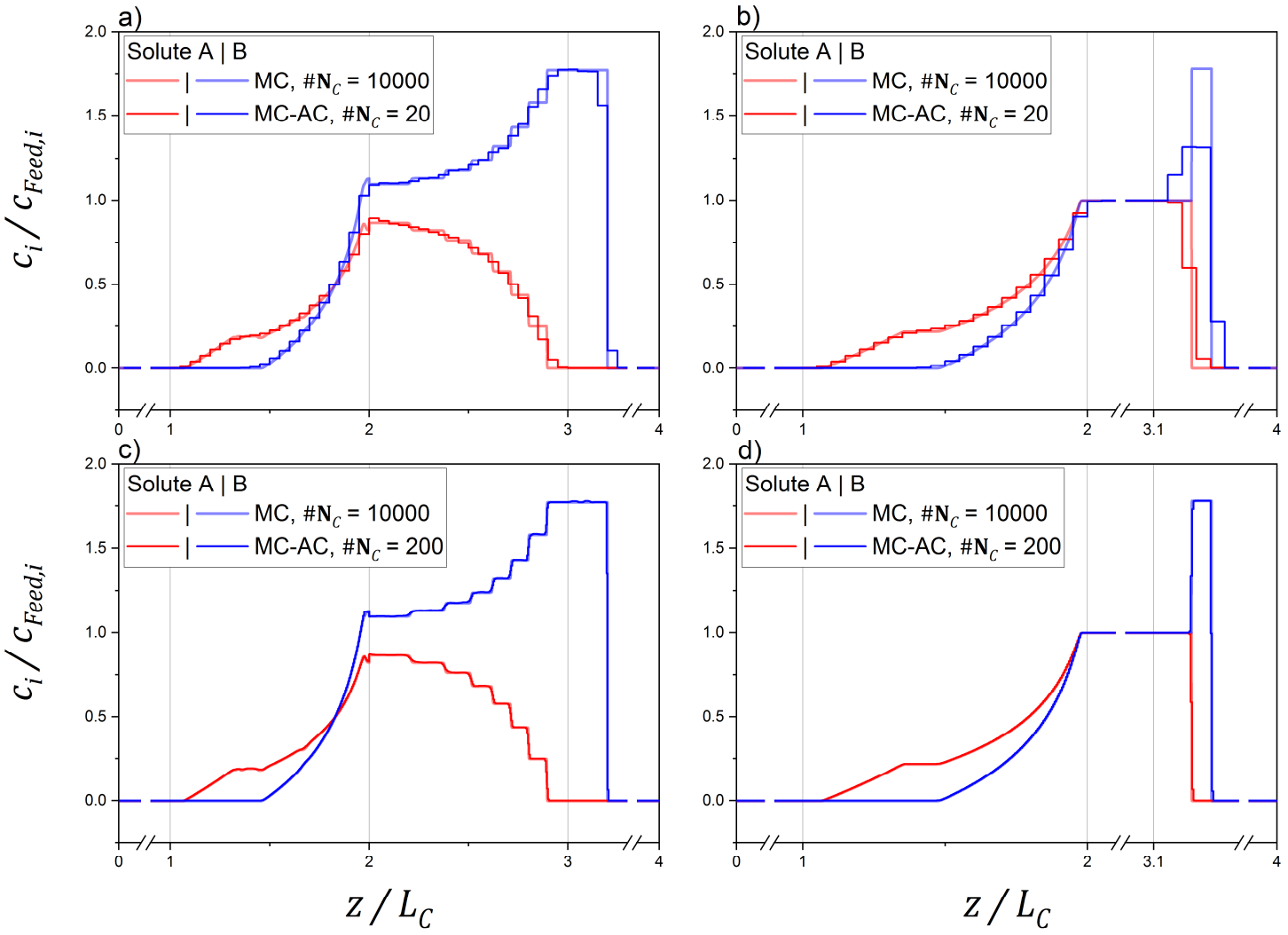

Figure 7.

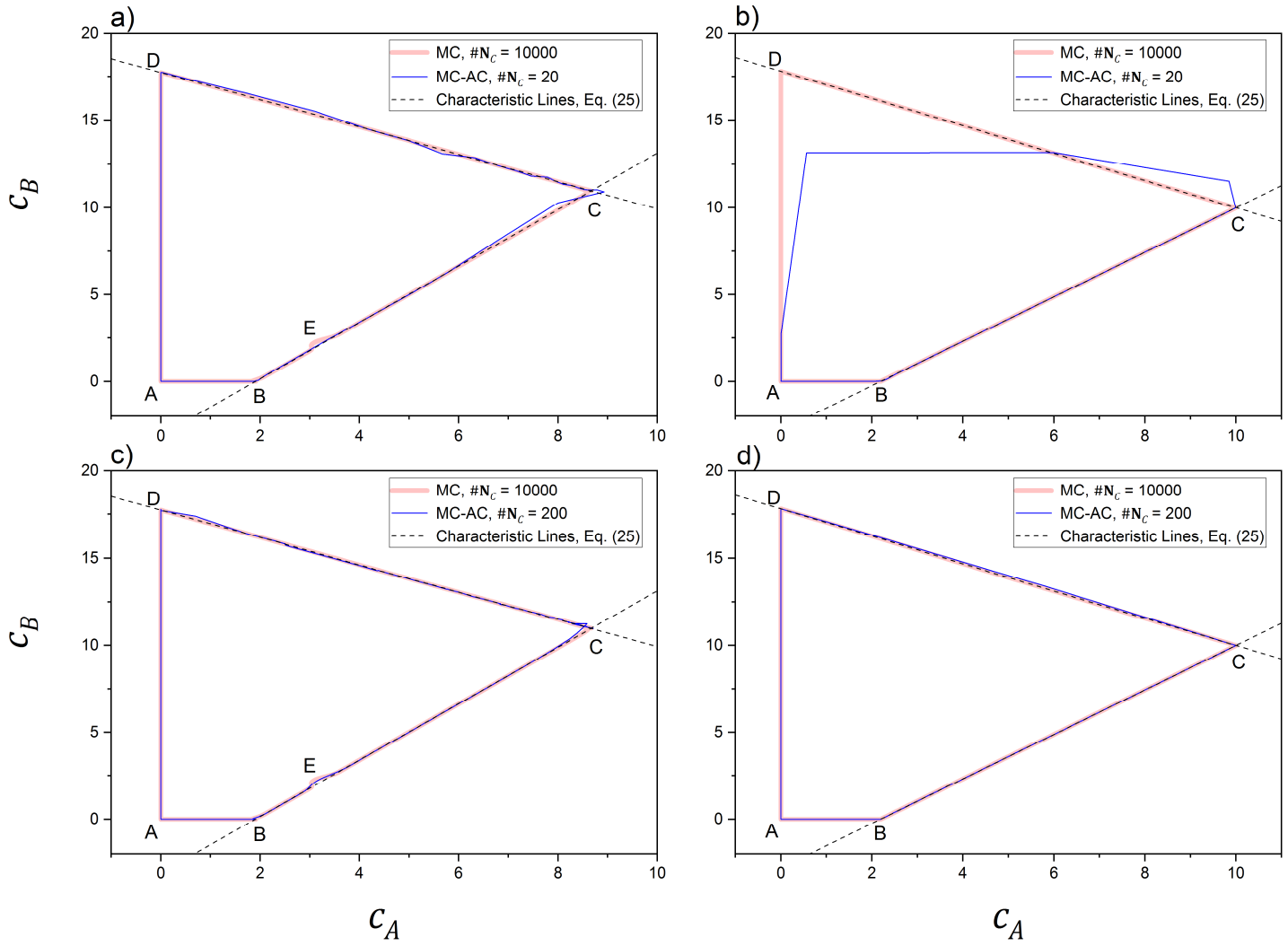
a)
b)
c)
d)
MC, #$\mathbf{N}_C$ = 10000
MC-AC, #$\mathbf{N}_C$ = 20
MC-AC, #$\mathbf{N}_C$ = 200
Characteristic Lines, Eq. (25)
A
B
C
D
E
c_B
c_A

Figure 8.

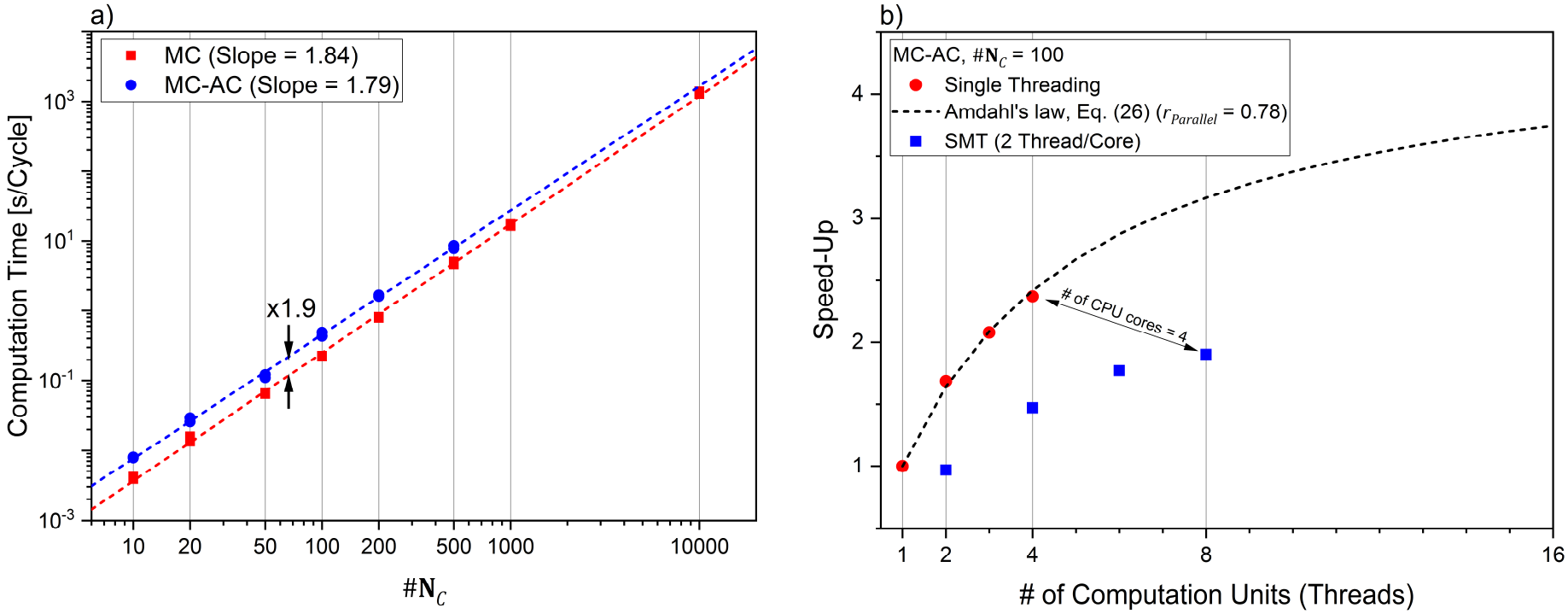
a)
MC (Slope = 1.84)
MC-AC (Slope = 1.79)
x1.9
Computation Time [s/Cycle]
10^{3}
10^{1}
10^{-1}
10^{-3}
10
20
50
100
200
500
1000
10000
$\#\mathbf{N}_C$
b)
MC-AC, $\#\mathbf{N}_C$ = 100
Single Threading
Amdahl's law, Eq. (26) ($r_{Parallel}$ = 0.78)
SMT (2 Thread/Core)
# of CPU cores = 4
Speed-Up
1
2
3
4
1
2
4
8
16
# of Computation Units (Threads)

Figure 9.

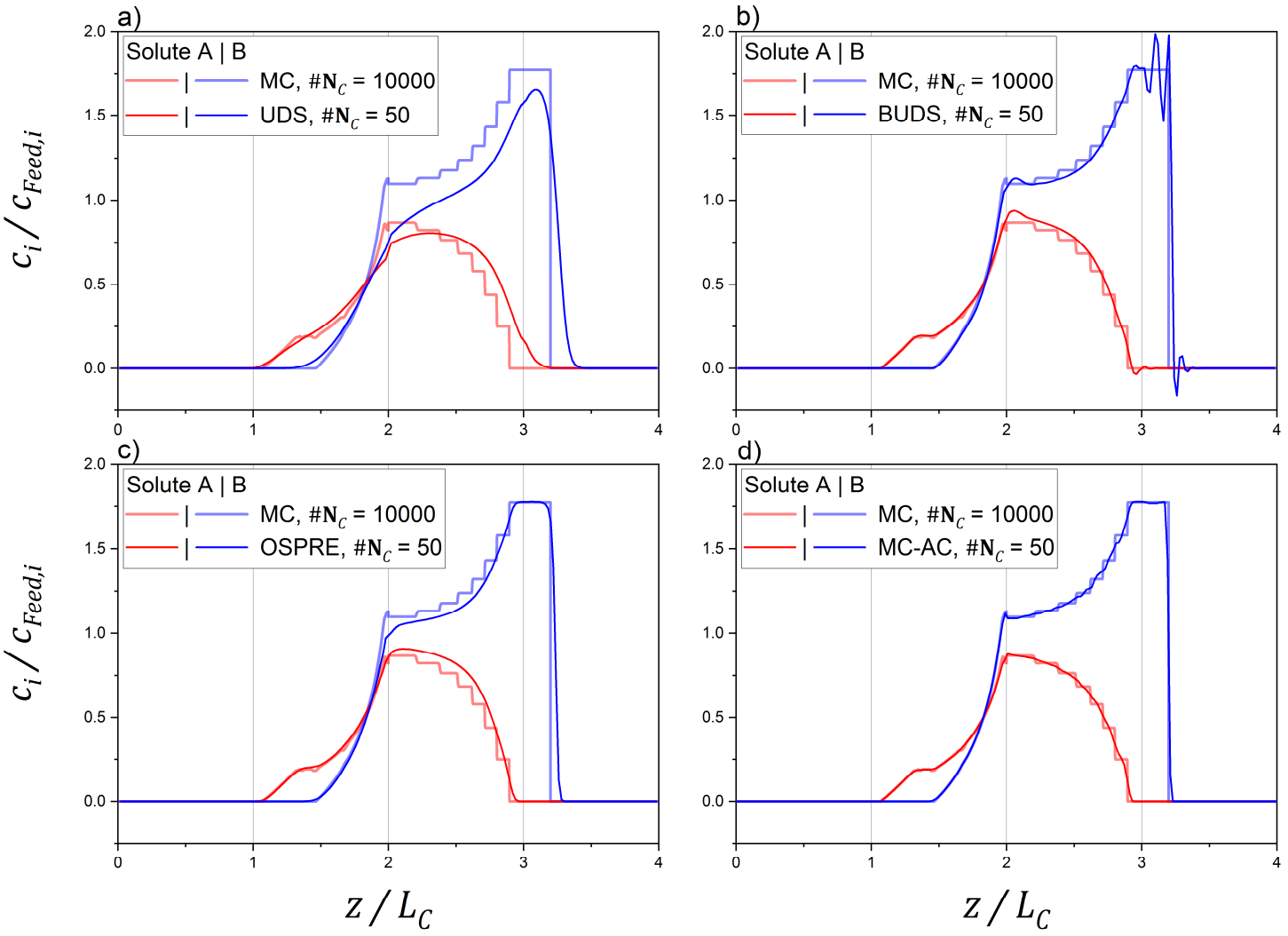
a)
Solute A | B
MC, #N_C = 10000
UDS, #N_C = 50
b)
Solute A | B
MC, #N_C = 10000
BUDS, #N_C = 50
c)
Solute A | B
MC, #N_C = 10000
OSPRE, #N_C = 50
d)
Solute A | B
MC, #N_C = 10000
MC-AC, #N_C = 50
c_i / c_Feed,i
z / L_C

a

Figure 10.

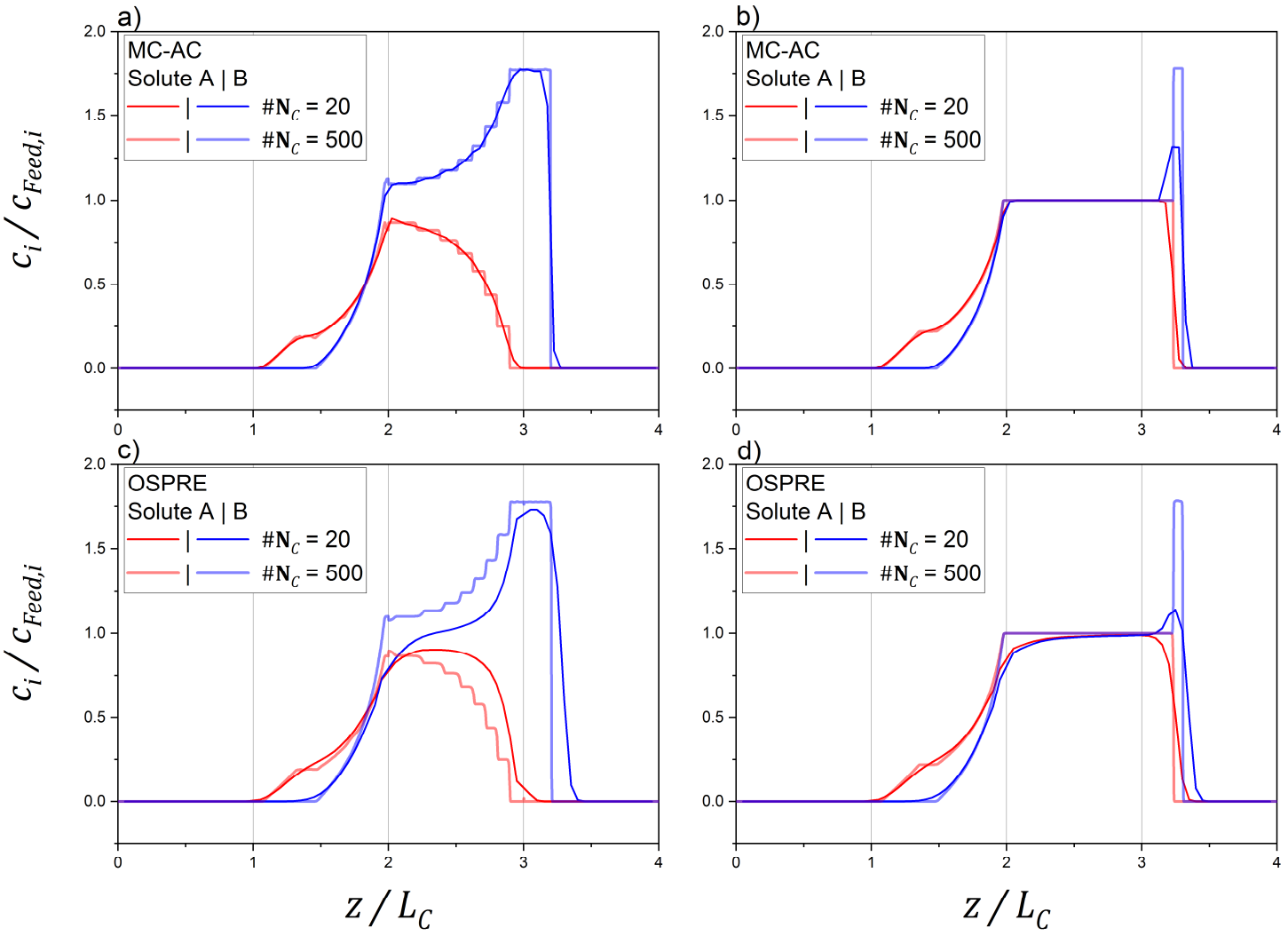
a)
MC-AC
Solute A | B
| #N_C = 20
| #N_C = 500
b)
MC-AC
Solute A | B
| #N_C = 20
| #N_C = 500
c)
OSPRE
Solute A | B
| #N_C = 20
| #N_C = 500
d)
OSPRE
Solute A | B
| #N_C = 20
| #N_C = 500
c_i / c_Feed,i
c_i / c_Feed,i
z / L_C
z / L_C

Figure 11.

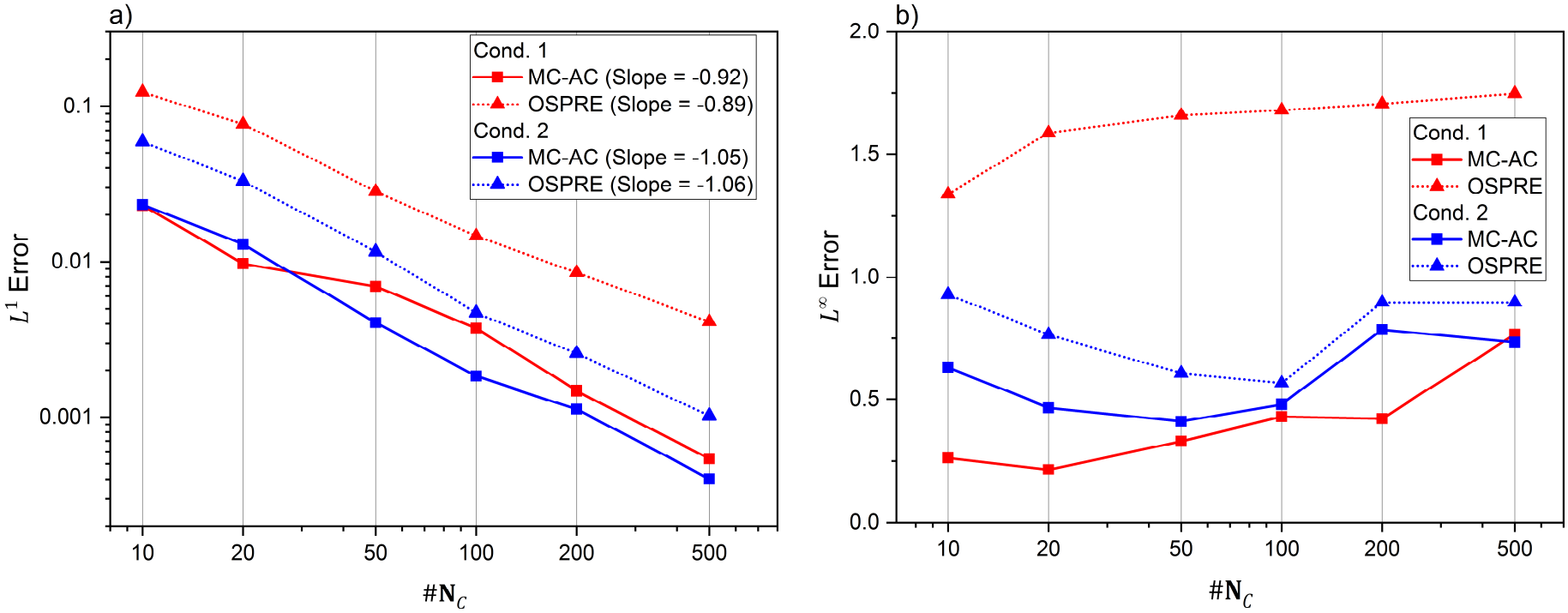
a)
Cond. 1
MC-AC (Slope = -0.92)
OSPRE (Slope = -0.89)
Cond. 2
MC-AC (Slope = -1.05)
OSPRE (Slope = -1.06)
0.1
0.01
0.001
L^1 Error
10
20
50
100
200
500
$\#\mathbf{N}_C$
b)
2.0
1.5
1.0
0.5
0.0
L^∞ Error
Cond. 1
MC-AC
OSPRE
Cond. 2
MC-AC
OSPRE
10
20
50
100
200
500
$\#\mathbf{N}_C$

Figure 12.

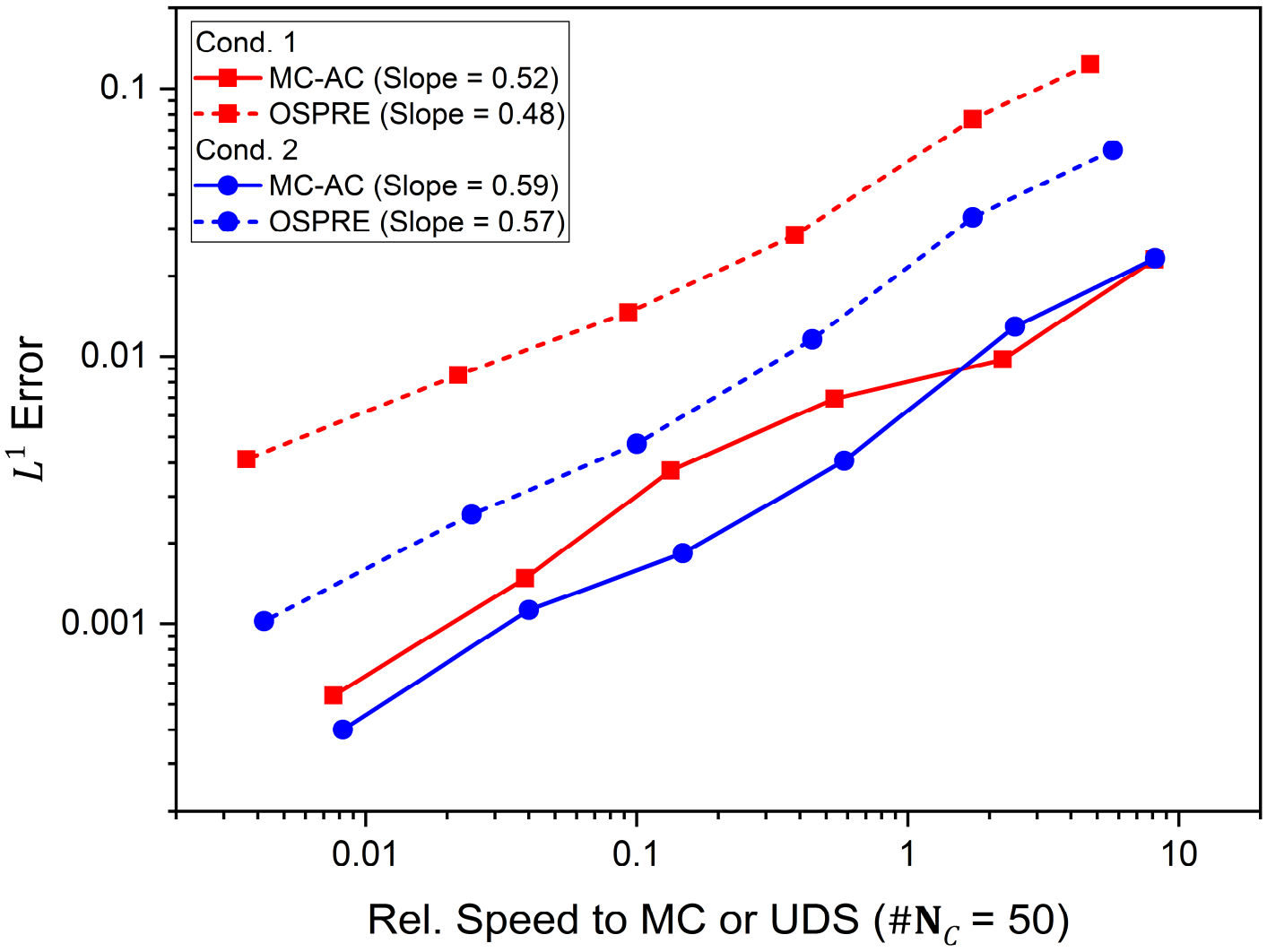
Cond. 1
MC-AC (Slope = 0.52)
OSPRE (Slope = 0.48)
Cond. 2
MC-AC (Slope = 0.59)
OSPRE (Slope = 0.57)
0.1
0.01
0.001
L^1 Error
0.01
0.1
1
10
Rel. Speed to MC or UDS (#$\mathbf{N}_C$ = 50)

Figure 13.

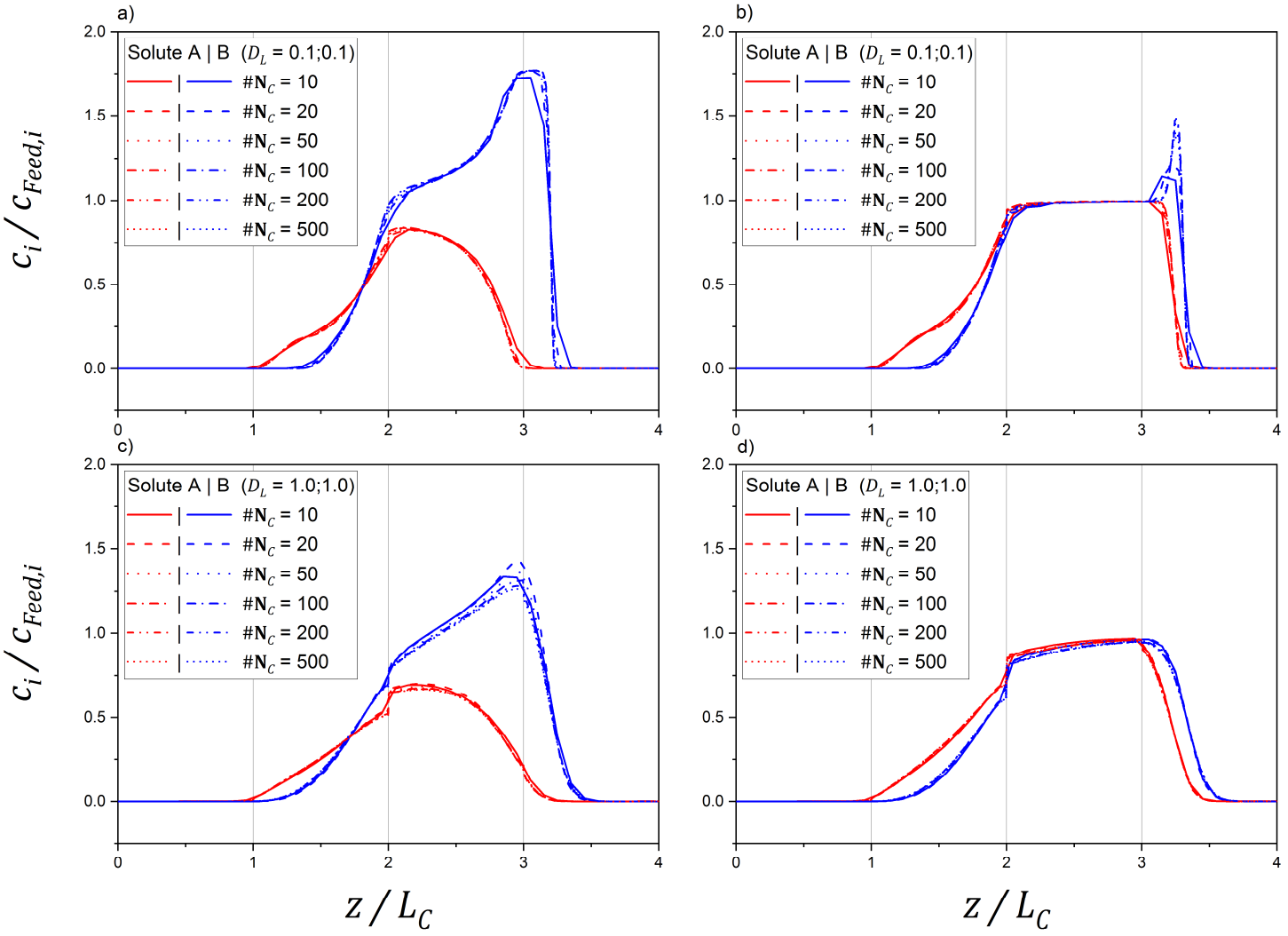
a)
b)
c)
d)
Solute A | B (D_L = 0.1;0.1)
Solute A | B (D_L = 1.0;1.0)
#N_C = 10
#N_C = 20
#N_C = 50
#N_C = 100
#N_C = 200
#N_C = 500
$c_i / c_{Feed,i}$
z / L_C

a

Figure 14.

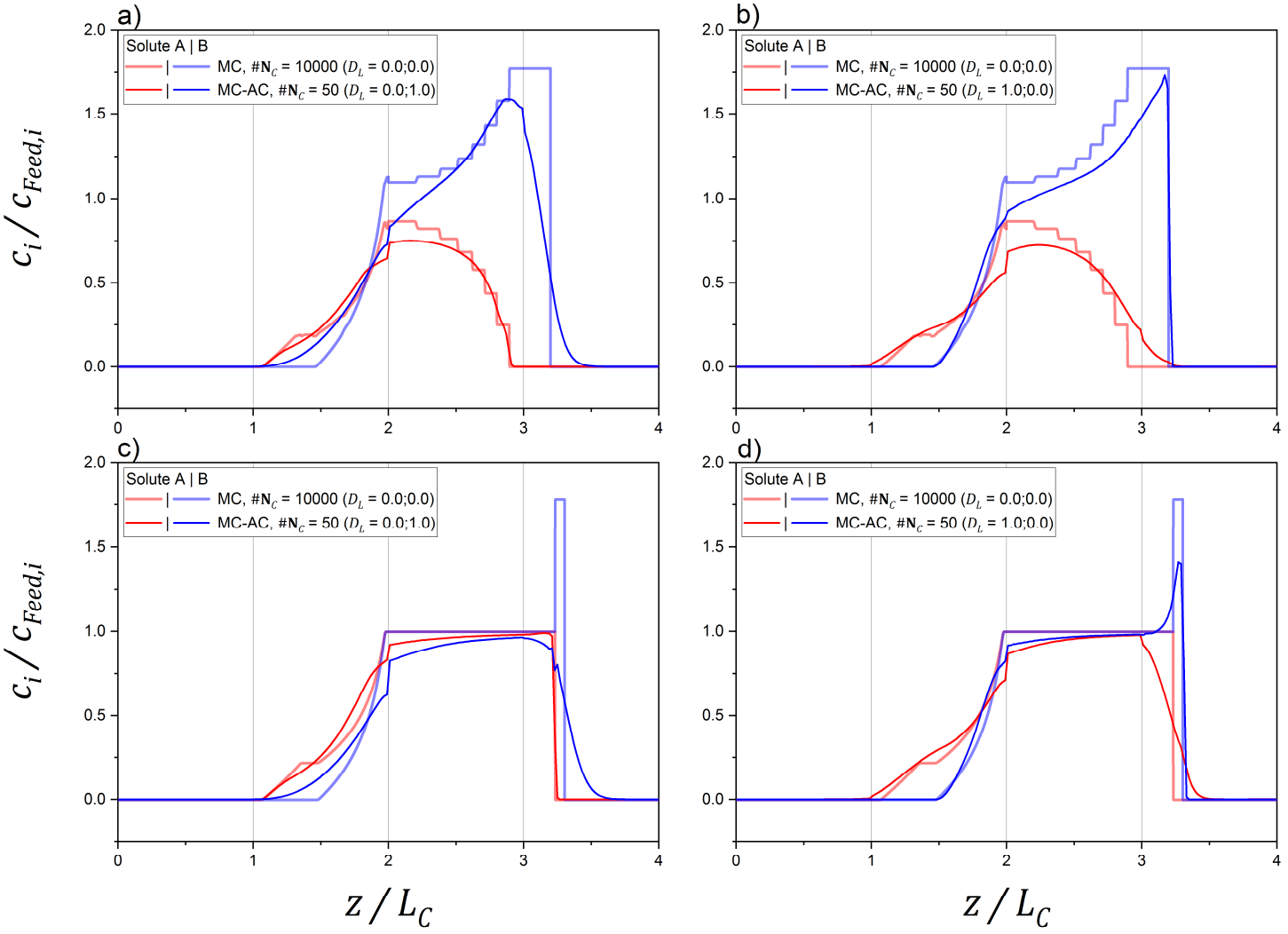
a)
b)
c)
d)
Solute A | B
MC, #N_C = 10000 (D_L = 0.0;0.0)
MC-AC, #N_C = 50 (D_L = 0.0;1.0)
MC-AC, #N_C = 50 (D_L = 1.0;0.0)
c_i / c_Feed,i
z / L_C

a

Figure 15.

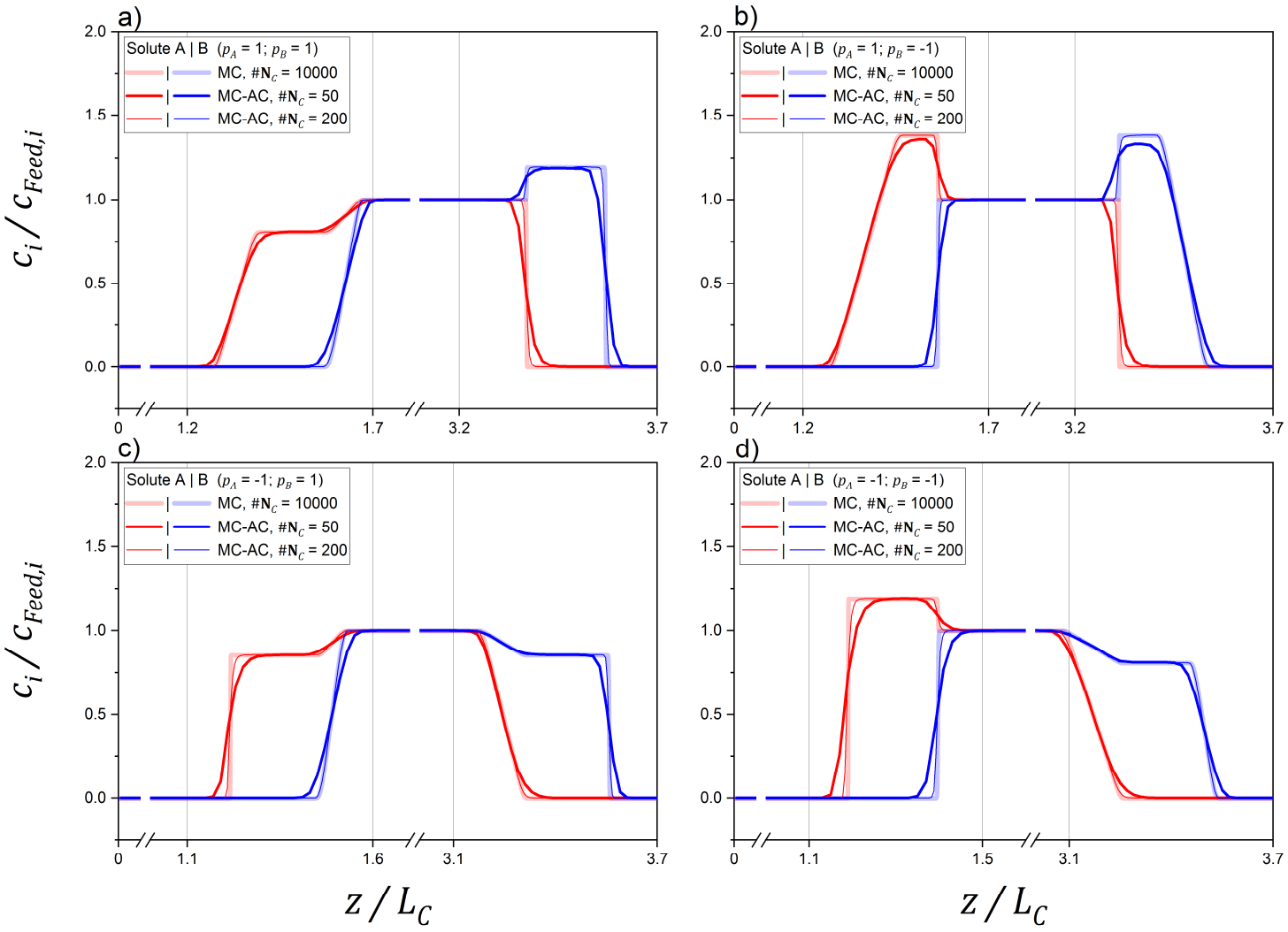
a)
b)
c)
d)
Solute A | B (p_A = 1; p_B = 1)
Solute A | B (p_A = 1; p_B = -1)
Solute A | B (p_A = -1; p_B = 1)
Solute A | B (p_A = -1; p_B = -1)
MC, #$\mathbf{N}_C$ = 10000
MC-AC, #$\mathbf{N}_C$ = 50
MC-AC, #$\mathbf{N}_C$ = 200
$c_i / c_{Feed,i}$
z / L_C
0
1.2
1.7
3.2
3.7
1.1
1.6
3.1
1.5
0.0
0.5
1.0
1.5
2.0

Figure 16.

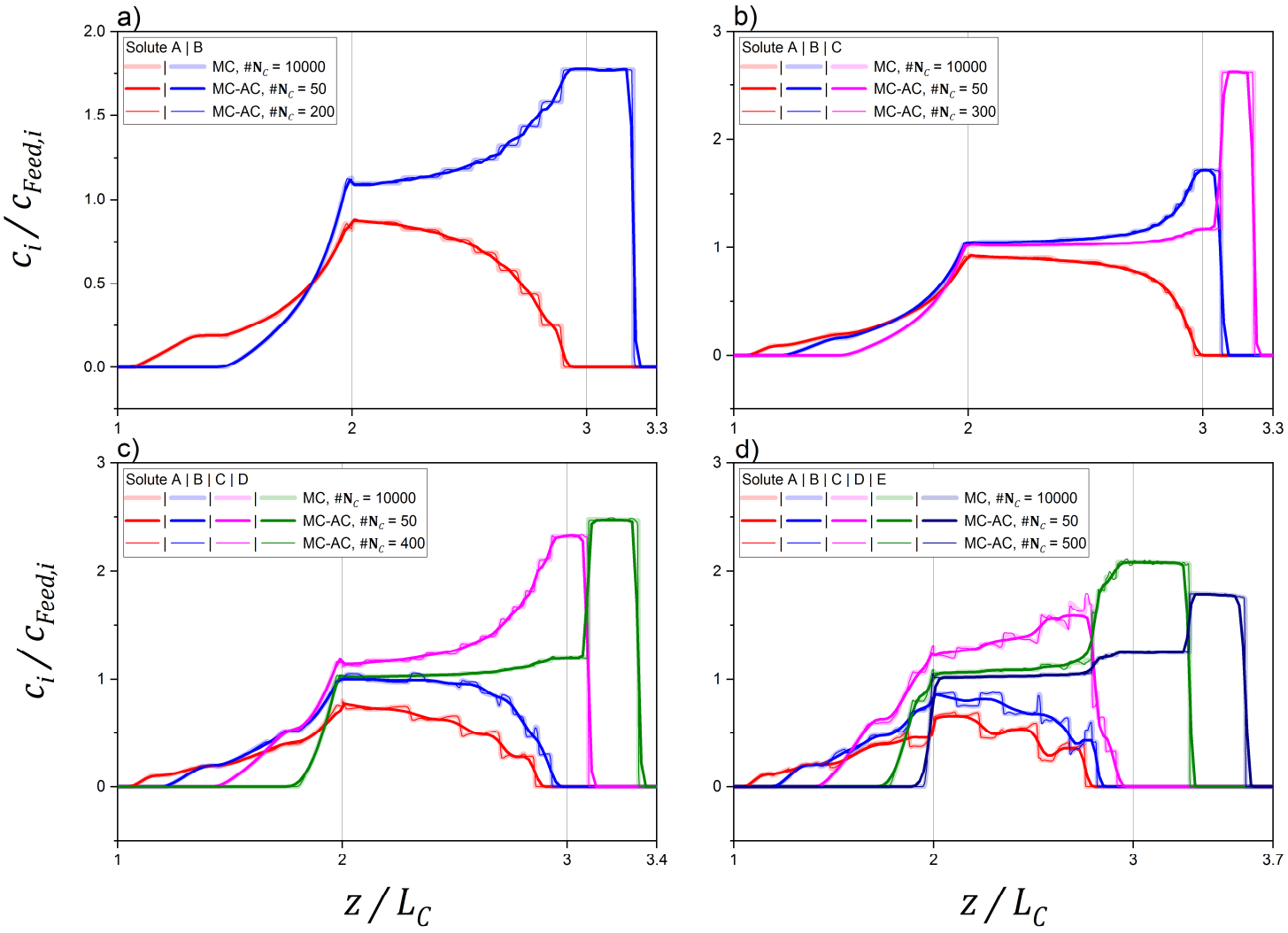
a)
Solute A | B
MC, #N_C = 10000
MC-AC, #N_C = 50
MC-AC, #N_C = 200
b)
Solute A | B | C
MC, #N_C = 10000
MC-AC, #N_C = 50
MC-AC, #N_C = 300
c)
Solute A | B | C | D
MC, #N_C = 10000
MC-AC, #N_C = 50
MC-AC, #N_C = 400
d)
Solute A | B | C | D | E
MC, #N_C = 10000
MC-AC, #N_C = 50
MC-AC, #N_C = 500
c_i / c_Feed,i
z / L_C